Solar Energy Materials & Solar Cells 298 (2026) 114164

Contents lists available at ScienceDirect

Solar Energy Materials and Solar Cells

journal homepage: www.elsevier.com/locate/solmat

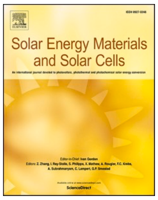

The dark side of certain POE encapsulant: Chemical pathways to metallisation corrosion in TOPCon modules

Chandany Sen [a,*], Haoran Wang [a], Robert Heidrich [b,c], Marius Lüdemann [b,c], Muhammad Umair Khan [a], Bram Hoex [a,**]

[a] *School of Photovoltaic and Renewable Energy Engineering, University of New South Wales, Sydney, NSW, 2052, Australia*
[b] *Fraunhofer CSP, Otto-Eißfeldt-Straße 12, Halle (Saale), 06120, Germany*
[c] *Anhalt University of Applied Sciences, Bernburger Strasse 55, Koethen (Anhalt), 06366, Germany*

ABSTRACT

N-type tunnel-oxide passivated contact (TOPCon) cell technology currently accounts for over 60 % of the PV market. Yet, its aluminium-rich front metallisation remains vulnerable to humidity-driven corrosion in glass/back-sheet modules. Building on our previous study, “Buyer Aware: Three new failure modes in TOPCon modules absent from PERC technology”, this work delves deeper into corrosion-induced degradation in TOPCon minimodules encapsulated with ethylene-vinyl acetate copolymer (EVA) and three commercially sourced polyolefin elastomers (POE-A, -B, and -C). After 1000 h of damp-heat exposure (85 °C, 85 % RH), the module with EVA showed a ~11 $\%_{rel}$ drop in P_{max}, mainly attributed to a 50 $\%_{rel}$ rise in series resistance (R_s). Spectroscopic analysis suggests that acetic acid released from EVA hydrolysis reacts with solder-flux residues, promoting front metal corrosion at the cell contacts. POE-A and POE-B modules degraded by only 6–10 $\%_{rel}$, neither produced measurable organic acids, and POE-A's antioxidant package appears to inhibit polymer oxidation, confining the residual loss to isolated pre-lamination contaminants. In contrast, POE-C suffered a 55 $\%_{rel}$ in P_{max}. Chemical probing reveals a potential cascade of mutually reinforcing reactions that generate a highly acidic micro-environment comprising: (i) carboxylic acids from POE oxidation, (ii) azelaic acid liberated from soldering flux, and (iii) benzoic and phenolic by-products from the ultraviolet (UV) absorber breakdown. This corrosive cocktail potentially accelerates the electrochemical attack on the front cell metallisation, driving a drastic R_s increase and catastrophic module failure. The study highlights the pivotal influence of encapsulant formulation, antioxidant, UV absorber chemistry and manufacturing cleanliness on the long-term reliability of TOPCon modules.

1. Introduction

The long-term stability of photovoltaic (PV) systems is paramount for reducing the levelized cost of electricity (LCOE) and ensuring sustainable energy production. For a PV system to be economically viable, it is expected to operate with minimal degradation, typically less than a 20 % relative performance loss, over a service life of 25–50 years [1]. In today's market, bifacial silicon tunnel oxide passivated contact (TOPCon) technology dominates, capturing the largest share thanks to its combination of high conversion efficiency and scalable manufacturability [2].

While TOPCon solar cells have achieved record-setting efficiencies, their long-term reliability is compromised by a susceptibility to degradation induced by humidity [3–11]. This vulnerability to the humidity becomes especially pronounced in modules that use a glass-backsheet design, which can accelerate performance loss. Field observations and accelerated aging tests show that TOPCon devices manufactured up to early 2024 were highly susceptible to moisture- and heat-driven corrosion of the front metallisation [3–6,8–13]. A major contributing factor was the use of silver (Ag) screen-printing pastes with a significant amount of aluminium (Al) [11–13]. During firing, finely dispersed Al helps disrupt surface oxides and promotes local Ag–Si contact formation (spiking), lowering contact resistivity [14,15]; however, the residual Al and Al-rich phases left within the sintered contact and glass-frit matrix are electrochemically active. Under humid and/or acidic and/or salt conditions, they depassivate, act as local anodes in galvanic couples with Ag, accelerate frit dissolution, and ultimately drive contact thinning, Pb/Ag migration, and an increase in series-resistance [13,16]. The recent adoption of laser-assisted contact firing, for example laser-enhanced contact optimisation (LECO), enables low-Al or Al-free Ag pastes without sacrificing contact resistivity; consequently, susceptibility to corrosion-induced degradation is markedly reduced [16]. However, recent work by Li et al. shows that corrosion-induced degradation in TOPCon cells remains a challenge, even with laser-assisted firing, if the contact firing temperature is not optimized [8].

---

* Corresponding author.
** Corresponding author.
E-mail addresses: Chandany.sen@unsw.edu.au (C. Sen), b.hoex@unsw.edu.au (B. Hoex).

https://doi.org/10.1016/j.solmat.2026.114164
Received 26 August 2025; Received in revised form 24 December 2025; Accepted 7 January 2026

The choice of encapsulant material is a crucial factor in mitigating moisture ingress and ensuring module longevity [3,9,10]. For years, ethyl-vinyl acetate copolymer (EVA) has been the industry standard [17]. However, its relatively high-water vapour transmission rate (WVTR) [10] and the tendency to produce corrosive acetic acid via hydrolysis under damp heat conditions presents significant reliability challenges [18–20], particularly for advanced cell architectures [9,10]. Consequently, polyolefin elastomer (POE) has emerged as a superior alternative. With its inherently low WVTR [10] and the absence of acetic acid hydrolysis [20–22], POE is widely regarded as the encapsulant of choice for high-reliability PV modules, especially in robust glass-glass configurations [10]. However, dual glass builds add weight, raise panel cost and increase breakage risk during handling and rooftop installation [2,23].

The push toward cost-effective glass–backsheet module designs has unexpectedly revealed severe and previously overlooked degradation pathways. Polyolefin elastomer (POE) encapsulants are generally regarded as more reliable than EVA due to their low moisture permeability and lack of acetic-acid generation. However, our recent study, “Buyer Aware? TOPCon's Reliability Issues in Comparison with PERC PV Modules after Damp Heat Testing”, challenged this long-standing assumption and received considerable attention in the photovoltaic community [3]. In that work, TOPCon modules encapsulated with a specific commercial POE formulation (POE-C) exhibited catastrophic power loss under damp-heat stress, degrading even more severely than their EVA-based counterparts. This surprising result directly contradicted the established perception of POE's protective qualities and suggested the presence of previously unidentified, chemically aggressive additives or degradation products in certain POE formulations [9,10]. These findings underscore that encapsulant reliability cannot be assumed uniformly across the POE class, highlighting the urgent need to investigate the chemical origins of such failures in greater detail.

Despite POE's growing adoption in photovoltaic modules, a critical knowledge gap persists regarding the chemical composition of specific formulations and the degradation mechanisms they may initiate. Building on our previous work, this study addresses that gap through a comprehensive investigation of three commercially available POE encapsulants, two shown to maintain TOPCon cell stability and one associated with severe performance degradation [3,4]. Using systematic chemical analyses and high-resolution microscopy, we identify a key additive linked to accelerated corrosion of the front metallisation. We further elucidate the corrosion pathway responsible for contact pitting and interfacial delamination, providing a clear mechanistic explanation for the substantial power loss observed.

2. Experimental method

2.1. Detail of encapsulant

Table 1 shows the encapsulant and polymer backsehet property provided by suppliers. All materials were sourced from different manufacturers. The encapsulant and backsheet materials exhibit distinct physical, optical, mechanical, and electrical characteristics that collectively determine module reliability and performance.

The surface structures of Encapsulant POE-A, B, and C are matte or embossed POE, aiding air removal during lamination, while the surface structure of EVA was not provided in the suppliers' datasheet. The widths and thicknesses define compatibility with various module formats, while high optical transmission (>90 %) ensures efficient light coupling. POE-C includes UV-cut features, while others (EVA, POE-A, and POE-B) remain fully transparent across the solar spectrum. Cross-linking level, expressed as gel content, varies across materials and may influence thermal stability and creep resistance. Dimensional stability during lamination is reflected in thermal shrinkage values, which generally remain low across POE grades and are slightly higher for EVA. Mechanical properties such as tensile strength and elongation indicate each material's ability to withstand thermo-mechanical stresses encountered during manufacturing and field exposure. Adhesion strengths, particularly to glass and backsheet surfaces, differ among encapsulants and influence the resistance to delamination under damp-heat and thermal cycling. Electrical insulation performance is highest in POE grades with very high-volume resistivity, supporting improved resistance to potential-induced degradation.

The backsheet, constructed as a multilayer PVF/PET/primer laminate, provides structural reinforcement, moisture protection, and dielectric insulation. Its mechanical strength, low heat shrinkage, and

Table 1
Detailed specifications of all encapsulants (EVA, POE-A, B, and C) and the polymer backsheet used in this work.

Encapsulant/ Backsheet	EVA	POE-A	POE-B	POE-C	Backsheet
Material Type	EVA (transparent)	POE (high-transparency)	POE (super high clear)	POE (transparent)	PVF//PET//Primer laminate
Surface Structure	Not listed	Matte/Embossed	Embossed	Inside Matt/Outside Embossed	Smooth (not embossed)
Width (mm)	900–1300	970–1300	200–2200	Up to 1240	Cut-sheet sizes per customer
Thickness	0.4–0.6 mm	0.4–0.8 mm	Target ±10 %	0.45–0.65 mm	PET 285 μm + PVF 25 μm + Primer 50 μm (Laminate 380 μm)
Optical Transmission	≥91 %	>90 % (1100–380 nm)	≥90 %	≥91 %	Reflectivity >75 % (400–700 nm)
UV Cut-off	None	None	None	360 ± 30 nm	Not listed
Gel Content (%)	≥80	>70	≥75	55–85	Not listed
Shrinkage	≤3 %	MD ≤ 4 %; TD ≤ 1.5 %	MD ≤ 2.5 %; TD ≤ 1.0 %	<2.5 % @160 °C	MD <1.0 %; TD <0.6 % (150 °C × 30 min)
Tensile Strength	Not listed	Not listed	MD ≥ 6 MPa; TD ≥ 5 MPa	13 ± 4 MPa	MD > 450 N/10 mm; TD > 400 N/10 mm
Elongation (%)	Not listed	Not listed	≥600	≥550	MD >120 %; TD >100 %
Adhesion to Glass (N/cm)	≥100	>60	≥60	≥75	Encapsulant adhesion >70 N/10 mm
Adhesion to Backsheet (N/cm)	≥100	>50	≥40	≥75	PET–Primer peel >6 N/15 mm
Volume Resistivity	$\geq 1 \times 10^{15}$ Ω cm	$\geq 1 \times 10^{15}$ Ω cm	$\geq 1 \times 10^{16}$ Ω cm	$\geq 1 \times 10^{17}$ Ω cm	Breakdown voltage >20 kV
WVTR	Not listed	Not listed	≤4.0 g/m^2·day	Not listed	<1.9 g/m^2·day (38 °C, 90 % RH)
Lamination Temp (°C)	Not listed	Not listed	145–155 (single); 135–140 → 145–150 (double)	155–160 (single or double)	Not applicable (non-melt film)
Vacuum Time (min)	Not listed	Not listed	5–10 (single); 7–10 (double stage 1)	6–10	Not listed
Pressing Time (min)	Not listed	Not listed	15–20 (single); 2–5 → 10–15 (double)	12–16	Not listed

strong primer-encapsulant bonding contribute to stable module packaging. Low water vapour transmission and high breakdown voltage ensure robust environmental and electrical protection, especially important for high-voltage system designs. Together, the encapsulant and backsheet properties shape the module's optical efficiency, mechanical durability, moisture resistance, and long-term electrical stability.

2.2. Minimodule fabrication

Bifacial n-type silicon TOPCon solar cells sourced from industry were used in this work; all these cells were fabricated around 2023 without laser-assisted firing. The TOPCon cells featured a boron-doped emitter (p^+ emitter), aluminium oxide (Al_2O_3)/hydrogenated silicon nitride (SiN_x:H) stack, and a screen-printed H-pattern silver/aluminium grid on the front. On the rear side, there was a silicon dioxide (SiO_2)/phosphorus-doped poly silicon (n^+poly-Si)/SiN_x:H stack and a screen-printed H-pattern silver grid. The solar cell schematic diagram is shown in Fig. 1a. All cells were soldered on both sides to connect ribbon/tabbing wires to the busbar of cells, creating an 8-cell string. Subsequently, all TOPCon cells were encapsulated with various bills of materials (BOM) to create module structures at an industrial facility.

The lamination process was carried out using a two-chamber, two-stage thermal process to ensure uniform encapsulant flow, effective degassing, and controlled cross-linking. In the first chamber, the module stack was heated to approximately 145 °C under vacuum, which reduces the viscosity of the EVA or POE encapsulant, promotes interfacial wetting between the glass, solar cells, and backsheet, and allows trapped air and volatile by-products to escape. This temperature is intentionally kept below the main cross-linking onset of the encapsulant to prevent premature gelation that could lead to void formation or incomplete interface contact. In the second chamber, the temperature is increased to around 155 °C to activate and complete the cross-linking reaction, thereby establishing strong adhesion and long-term mechanical and environmental stability of the laminated module. A total lamination duration of approximately 20 min was applied and was sufficient to achieve homogeneous heat transfer through the module thickness and an adequate degree of curing. This temperature-time profile lies within the processing window typically recommended for commercial EVA and POE encapsulants, as listed in Table 1. All modules underwent DH test at 85 °C and 85 % relative humidity (RH) for up to 1000 h to study humidity-induced failures. Fig. 1(b) and (c) provide a detailed experimental flow diagram for this work and the PV module configuration in this study.

2.3. Characterisation

Module performance was measured before and after 1000 h of DH exposure under standard test conditions (25 °C, AM 1.5 G, 1000 W m^2) using a commercial flash tester (Eternalsun Spire 5600SLP Blue, Spi-Sun Simulator™). Line scan electroluminescence (EL) imaging was performed to assess spatially resolved defects in the samples before and after DH testing, using a BTi-M1 line-scan EL system. Constant current injection of 6 A and a scanning speed of 80 mm/s were maintained to enable direct comparison between measurements.

Aged mini-modules were sectioned with abrasive-waterjet cutting into ~2 cm × 2 cm tokens centred on the visually affected areas. These tokens were then heated on a hot plate at 85 °C to soften the encapsulant; solar cells and polymer films were then gently separated using tweezers to avoid mechanical damage. Chemical changes in pristine and damp-heat aged encapsulant films were examined using attenuated total reflection Fourier-transform infrared spectroscopy (ATR-FTIR, PerkinElmer Spectrum 100). Spectra were collected over the range 4000–650 cm^{-1} with 8 scans per sample at a resolution of 4 cm^{-1}. Air spectra were recorded and subtracted as background. Encapsulant samples were measured from the front side of the modules, either from the portion adhering to the glass or from the portion adhering to the solar cells. Raw spectra were processed using PerkinElmer UV WinLab software. An interactive baseline correction (i-baseline) was applied to minimise background artefacts. No peak normalisation was performed; therefore, the comparison of spectra is based on qualitative differences in band appearance and relative intensity changes rather than absolute intensity scaling. X-ray photoelectron spectroscopy (XPS) was used to analyse the surface chemistry of the Ag metallisation on both fresh cells and cells removed from DH-aged modules, using a Thermo ESCALAB 250Xi X-ray photoelectron spectrometer (Al Kα, 1486.7 eV, 120 W, 500 μm spot size). Spectra were charge-corrected using the C 1s peak of adventitious carbon at 284.8 eV. A Zeiss 550 Crossbeam FIB-SEM was utilised to perform scanning electron microscopy (SEM) on the Ag metal contacts of both a fresh, unaged solar cell and a cell extracted from the most degraded module. The analysis was conducted at an accelerating voltage of 5 kV to acquire high-resolution images of the contact surfaces. To determine the elemental composition of the contacts, energy-dispersive X-ray spectroscopy (EDS) was carried out using an Oxford Instruments detector and analysed with the Aztec software package. The characteristic X-ray lines used for elemental identification were selected based on their energy and the absence of peak overlaps. Specifically, the L-shell was used for Ag and zinc (Zn), the K-shell for oxygen (O) and Al, and the M-shell for lead (Pb). The selection of these specific electron shells for evaluation is determined by the atomic number (Z) of each element and the optimal energy range for detection and resolution by the Si drift detector [24].

The chemical composition of additives in the encapsulant materials was analysed using Pyrolysis-Gas Chromatography-Mass Spectrometry (Py-GC/MS). The analytical system consisted of an EGA/PY-3030D pyrolysis furnace equipped with an AS-1020E autosampler (Frontier Laboratories Ltd.) coupled to a Thermo Scientific Trace 1300 Gas Chromatograph and an ISQ7000 Mass Spectrometer. Chromatographic separation was achieved using an Ultra Alloy Capillary Column (30 m length, 0.25 mm internal diameter, 0.25 μm film thickness; Frontier Laboratories Ltd.) with helium as the carrier gas at a constant flow rate.

Based on previous work, a single-stage thermal desorption (TD) was carried out [25]. The sample was placed in the pyrolysis oven, which had been preheated to 100 °C, using an autosampler. Immediately after

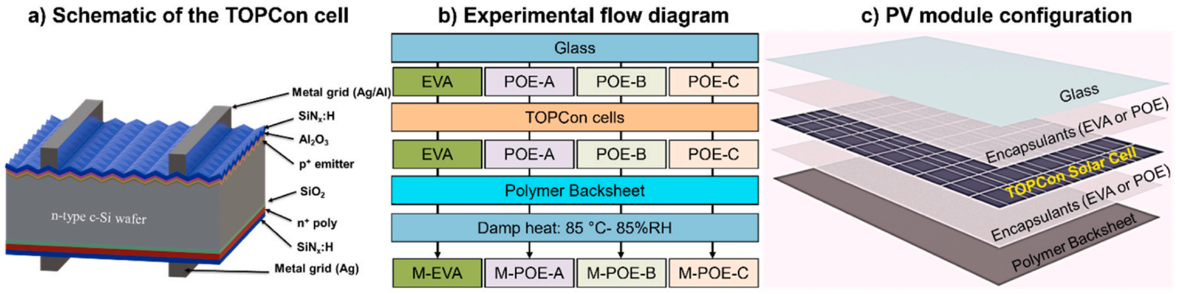

Fig. 1. a) schematic of TOPCon solar cells, b) experimental flow diagram, c) PV module configuration used in this study.

the sample was placed in the oven, the temperature was ramped up at a rate of 30 K/min until it reached 300 °C. After desorption in the pyrolysis oven, the volatile molecules pass into the GC. This was held at 40 °C for 1 min and then heated to 325 °C at 10 K/min. The final temperature was maintained for 20 min. The MS was set to the m/z range 29–800 and previously tuned to the characteristic m/z (219) peak of the calibration substance [m/z (219) ~ 2e7].

Throughout the analysis, the interface temperature between the pyrolyser and the GC inlet was maintained at 100 °C above the current pyrolysis oven temperature to prevent condensation of the analytes. For sample preparation, encapsulant materials were physically extracted from the front and rear sides of the modules. Small samples (~2–4 mg) were prepared by layer-by-layer separation using a scalpel, starting from the backsheet and weighed on a Mettler Toledo XS205DU microbalance (resolution: 0.01 mg). Given the precision of the balance relative to the sample mass, the weighing error was considered negligible.

3. Results and discussion

3.1. Module testing results

Fig. 2 illustrates the relative changes in I-V parameters for modules with different BOM following 1000 h of DH testing. Among the different encapsulants, the POE-C module (M-POE-C) was found to be the least stable, with its maximum (P_{max}) and fill factor (FF) decreasing by ~50 $\%_{rel}$. In comparison, the P_{max} and FF of the module with EVA (M:EVA) degraded by ~11 $\%_{rel}$, while the modules with POE-A and POE-B (M: POE-A and M:POE-B) showed P_{max} reductions of 15.6 $\%_{rel}$ and ~6 $\%_{rel}$, respectively. The primary mechanism for power loss across all modules was a one to three order of magnitude increase in series resistance (R_s). Correspondingly, open-circuit voltage (V_{OC}) and short-circuit current (I_{SC}) were largely unaffected, with one exception. The severe I_{SC} drop observed in the POE-C module is attributed to its exceptionally high post-aged test R_s, which hindered effective charge carrier collection. A similar effect is often observed in our previous work, where I_{SC} experiences a significant reduction whenever high R_s significantly impacts a solar cell or module [11,26,27].

Fig. 3 displays the EL images for each module, revealing distinct post-aged failure modes. A widespread decrease in EL intensity was observed across the modules. However, it is noted that the photoluminescence (PL) intensity was found to increase for all cells after DH testing (data not shown). An increase in PL in combination with a reduction in EL intensity suggests the cells' intrinsic radiative efficiency remained high. Therefore, the degradation in EL intensity is not due to recombination but is primarily attributed to an increase in R_s, which limits current injection [28]. These EL results aligned well with the changes in I-V measurements presented in Fig. 2.

The specific failure modes were dependent on the encapsulant material used. For instance, the EVA-encapsulated module (M: EVA) exhibited EL signal loss concentrated at the solder interconnections, a pattern characteristic of electrochemical corrosion triggered by acetic acid generated from EVA hydrolysis and catalysed by solder-flux residues, as widely documented for EVA-based PV modules [10,27,29].

The module with POE-A (M: POE-A) exhibited a localised drop in EL intensity, which corresponds to an increase in R_s, as reported in our previous work [3,4]. This failure was likely caused by contaminants (such as Na^+, Ca^{2+}, Mg^{2+}, Cl^-, S^{2-}) present on the solar cell prior to encapsulation, which corroded the metal contacts upon moisture ingress [4]. The results suggest the additive in POE-A did not have a detrimental impact; this was confirmed by fabricating a replicate module with minimised contaminant exposure, which showed a P_{max} loss of only ~0.03 $\%_{rel}$ [4].

Similar to the POE-A module, the module with POE-B (M: POE-B) also exhibited localised loss in EL intensity, though to a lesser extent. This module also showed an EL intensity drop along the solder interconnections, similar to the M: EVA module. These observations suggest that chemical interactions between moisture, soldering flux, and cell metallisation increased R_s, thereby reducing P_{max} [13]. The combined findings for the POE modules suggest that additives from POE-A and POE-B are likely not to play a primary role in the observed power loss.

However, the module with POE-C (M: POE-C) experienced a severe and widespread loss of EL intensity across the entire minimodule. Although the degradation mode initially resembled that of other modules with other BOM, which initiated at the ribbon-to-busbar interconnections, its progression was exceptionally rapid [3]. As shown in our previous work on the same module (T5), this failure began after 500 h of DH testing before propagating across the entire cell area, culminating in the observed ~50 $\%_{rel}$ power loss after 1000 h of DH testing [3]. Given that the rate of degradation was far greater than in any other module in this study, it is strongly suggested that an additive in the POE-C encapsulant, likely in combination with the soldering flux, may play a critical role in accelerating this failure mechanism.

3.2. Encapsulant materials analysis

As illustrated above, the data reveal distinct degradation pathways that vary according to the encapsulant material. The EVA-encapsulated module showed degradation primarily concentrated along the ribbon-to-busbar interconnections of the TOPCon cells. In contrast, the

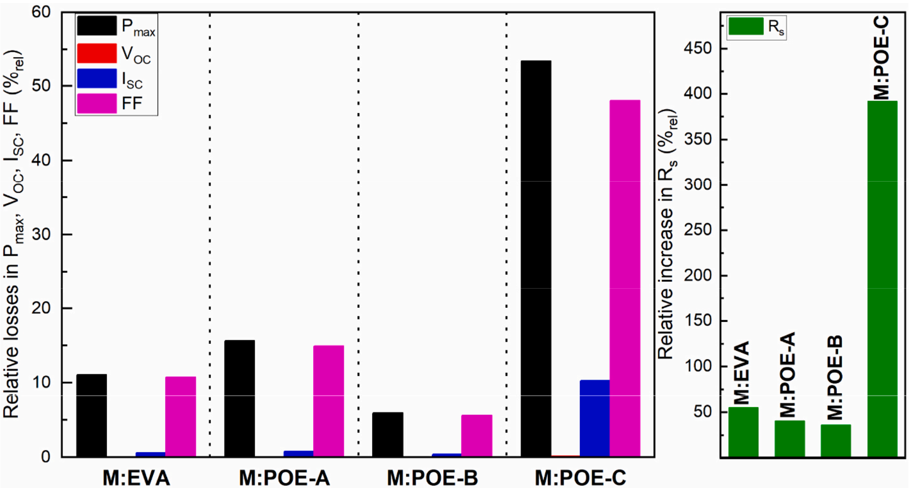

Fig. 2. Relative losses in P_{max}, V_{OC}, I_{SC}, and FF (left), and the corresponding increase in R_s (right) observed after 1000 h of DH testing.

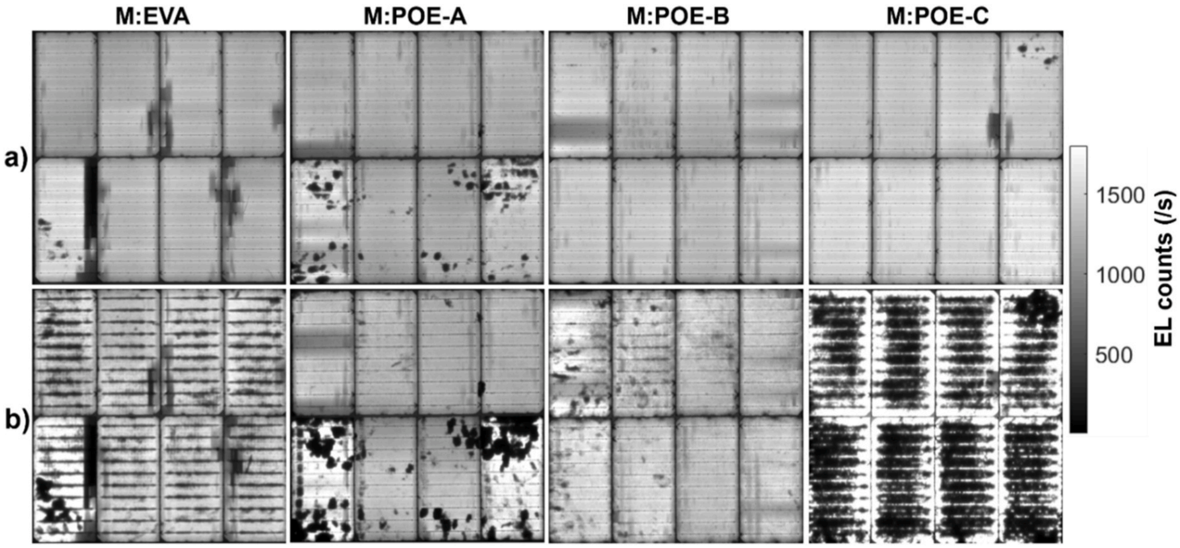

Fig. 3. EL images of modules with EVA (M: EVA), POE-A (M: POE-A), POE-B (M: POE-B), and POE-C (M: POE-C), captured (a) before and (b) after 1000 h of DH testing.

degradation observed in the POE-A and POE-B modules was less severe around the solder interconnections and appeared to be driven more by pre-existing surface contaminants rather than an intrinsic material failure, indicating a negligible role for the POE-A and POE-B additives in the observed power loss. The POE-C module, however, exhibited significantly more severe and rapid degradation than all other modules. Consequently, due to their unique failure signatures, all encapsulants underwent further chemical and additive analysis.

Figs. 4 and 5 present the results of ATR-FTIR spectroscopy, which highlight the chemical changes that occurred in the EVA and POE encapsulants following DH testing. For comparison, the spectra of fresh EVA and POE-A (immediately after lamination but before DH testing) are also included as a reference alongside the aged encapsulant. Fig. 4 provides a full spectral overview for comparison, while Fig. 5 offers magnified views of the critical O-H stretching region (4000-2600 cm^{-1}) and the carbonyl/fingerprint region (1950-900 cm^{-1}) to highlight specific molecular changes [19,30].

The comparison between fresh and aged EVA reveals clear signs of chemical degradation. Fresh EVA exhibits the characteristic peaks of its copolymer structure, including prominent methylene (CH_2) C–H stretching vibrations at ~2919 and ~2851 cm^{-1}, a strong carbonyl (C=O) ester peak at ~1737 cm^{-1}, and C–O stretching bands at ~1237 and ~1020 cm^{-1} [18–20]. The spectra of the Aged_EVA show a broad O–H stretching band at ~3444 cm^{-1}, indicative of moisture absorption [19,31], accompanied by reduced intensities of the ester-associated C=O and C-O peaks. This reduction, together with the emergence of O-H absorption, is consistent with hydrolysis, in which water cleaves ester linkages in the vinyl acetate groups, forming hydroxyl functionalities and releasing acetic acid [18,22]. Such hydrolytic degradation is a well-known degradation pathway for EVA under heat and humidity, with the acetic acid generated likely contributing to metallic contact corrosion, leading to R_s increase within photovoltaic modules, as shown in Figs. 2 and 3, resulting in an ~11 $\%_{rel}$ power loss after DH testing.

In contrast, the POE materials exhibited widely different stabilities. The spectrum of Fresh_POE-A serves as the baseline and shows the characteristic peaks of a polyolefin, which is primarily composed of a polyethylene backbone. The most prominent features are the strong asymmetric and symmetric stretching vibrations of methylene (CH_2) groups at ~2918 cm^{-1} and 2850 cm^{-1}, respectively [20–22]. Other fundamental peaks include the CH_2 bending (scissoring) vibration at ~1463 cm^{-1} and the CH_2 rocking vibration at ~720 cm^{-1} [20,21]. The POE-A and POE-B formulations remained stable, with aged spectra nearly identical to the fresh reference (POE-A) and showing no significant formation of new O-H or carbonyl peaks. These results are consistent with literature reports demonstrating the chemical stability of POE, which effectively prevents moisture ingress into solar cells and thereby mitigates degradation [18,22].

On the other hand, the aged POE-C sample shows severe chemical change: a pronounced O–H stretch (~3440 cm^{-1}) indicative of moisture uptake [19,31] and three new carbonyl-region features (i) a ~1710 cm^{-1} C=O band attributable to carboxylic acids [32], (ii) a strong ~1571 cm^{-1} band characteristic of carboxylates/carboxylic acid salt (R–COO$^-$), and (iii) a ~1442 cm^{-1} band commonly assigned to metal–carboxylates [33–38]. Similar carboxylate/acid signatures after damp-heat have been reported at glass interfaces in EVA-based modules and in POE glass/glass laminates, although their origin was not analysed [39–41]. Their prominence at glass interfaces is consistent with interfacial chemistry, moisture uptake and alkali-ion leaching from soda-lime glass. In our glass/backsheet laminates, however, the ~1571 cm^{-1} band is not restricted to the glass side; it is also observed in regions adhered to the glass, the cell, the backsheet, and even in POE residues that leaked out at the module edges, indicating a formulation-specific oxidative/hydrolytic pathway, likely modulated by the additive/stabiliser package, that generates carboxylic acids and their metal salts. While the precise identities and precursors of these acids in POE-C remain unresolved, the FTIR signatures provide a mechanistic link between POE-C chemistry, interfacial reactions, the rise in R_s, and the substantial power loss observed after DH.

It is important to note that no as-received POE-C film was available for this study. The entire batch originally supplied was laminated into modules at the industrial fabrication site, and the remaining POE-C stock was subsequently discarded following severe failures observed during damp-heat testing. Despite repeated requests from the POE manufacturer, no additional fresh POE-C material could be obtained. Consequently, IR measurements for POE-C could only be performed on samples extracted from aged modules.

Fig. 6 displays Py-GCMS additive profiles for fresh POE-A (non-lamination) and DH aged POE-A, POE-C, and EVA, showing normalised intensities of six key additives: peroxide fragments (derived from crosslinking initiators, detected indirectly via 1-hexanol, 2-ethyl- signals formed when the labile O–O bond cleaves at ~115 °C) [42], triallyl isocyanurate (TAIC, a co-agent that reacts with macroradicals via allyl groups to enhance crosslink density and thermal resistance), hindered-amine light stabilisers (HALS, regenerating nitroxyl radical

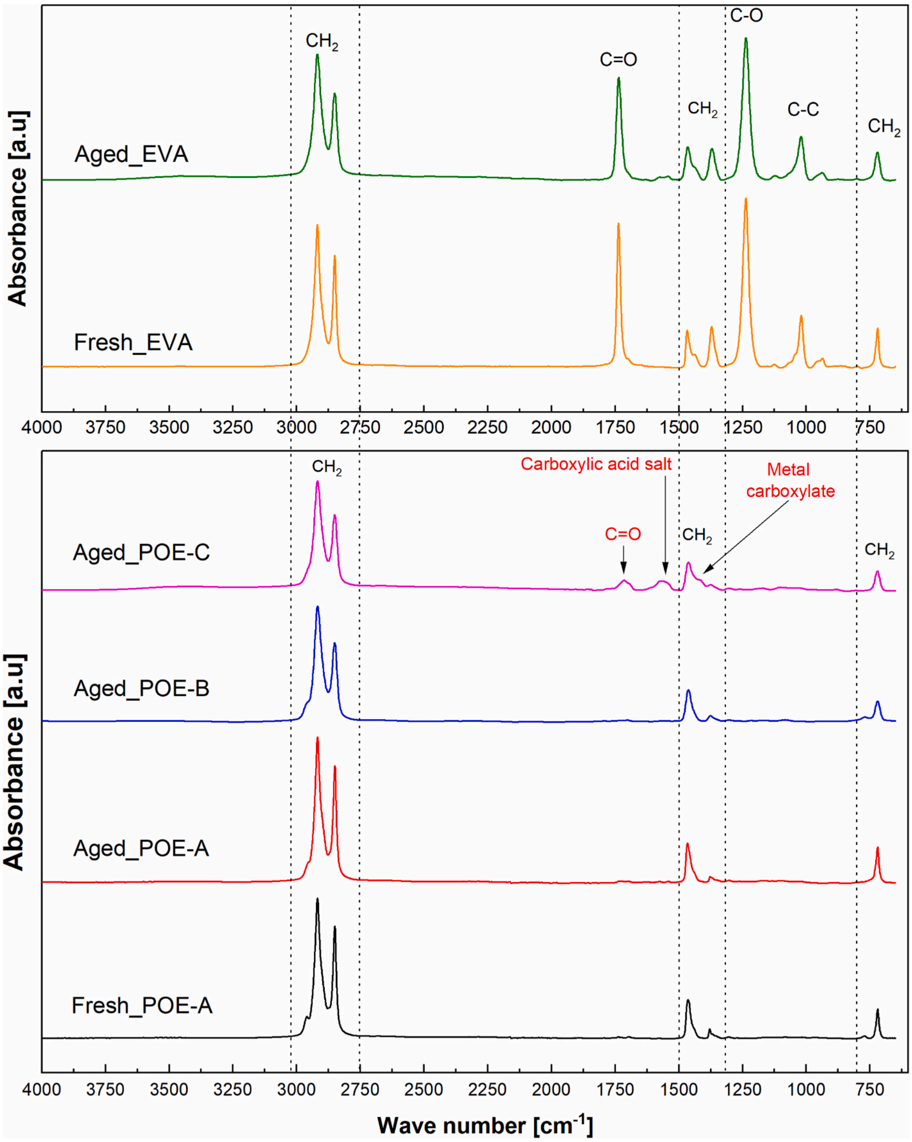

Fig. 4. ATR-FTIR spectra of fresh and aged encapsulants, including fresh EVA, fresh POE-A, aged POE-A, POE-B, and POE-C. Spectra of the fresh materials are included to facilitate direct comparison with their aged counterparts.

scavengers that prevent UV embrittlement), benzophenone UV absorbers (sacrificial UV shields), phosphites (hydroperoxide-decomposing antioxidants), and phosphates (inert byproducts of phosphite oxidation), common additive types used in PV encapsulant [18,25,43,44].

In fresh POE-A, a strong HALS signal (~2.7×10^7 a.u.) dominates. Residual peroxide, TAIC, and distinct phosphite/phosphate peaks indicate that crosslinking is essentially complete post-lamination. The phosphite profile is consistent with tris(2,4-di-tert-butylphenyl) phosphite (Irgafos 168), a processing stabiliser that provides short-term hydroperoxide control during melt/lamination and is designed to be sacrificial. After DH ageing, POE-A still exhibits a substantial HALS level (on the order of 10^7 a.u.), whereas the phosphite peak is markedly reduced and phosphate does not accumulate, consistent with (i) rapid phosphite consumption in ROOH reduction and (ii) subsequent hydrolysis at the phosphorus–oxygen–aryl (P–O–Ar) linkage that cleaves phosphite/phosphate aryl esters. HALS can undergo some loss under DH, including hydrolysis, yet the residual HALS level remains sufficient to suppress radical chain propagation. Notably, the polyethylene backbone itself is not susceptible to hydrolysis; in unstabilised PE at comparable temperatures, degradation proceeds via thermo-oxidation with finite induction times that shorten from ~months at ~70 °C to a few hundred hours at ~90 °C [45–47]. Together with low peroxide levels, this additive signature indicates that the stabiliser package functioned as intended, phosphite provided early peroxide control and HALS sustained long-term protection, explaining POE-A's negligible power loss. ATR-FTIR (Figs. 4 and 5) corroborates this: spectra remain essentially unchanged from the fresh state, with no growth of carbonyl (C=O) or hydroxyl (O–H) bands, evidencing minimal thermo-oxidative or hydrolytic degradation.

DH-aged EVA exhibits a distinct degradation profile. Py-GCMS shows only a modest phosphate signal and low peroxide levels, indicating a limited antioxidant package typical of legacy EVA formulations [25,44]. ATR-FTIR (Figs. 4, 5a and 5c) corroborates this pathway: the ester-associated C=O and C–O bands decrease in intensity (~1737 and ~1237/1020 cm^{-1}), while a broad O–H band emerges (~3440 cm^{-1}). These changes are consistent with the hydrolysis of the vinyl acetate groups and subsequent acetic acid formation. The resulting acidic environment plausibly promotes corrosion of the cell metallisation, aligning with the observed ~11 $\%_{\text{rel}}$ power loss and ~50 $\%_{\text{rel}}$ rise in R_s after DH testing.

The catastrophic failure of aged POE-C appears formulation-driven.

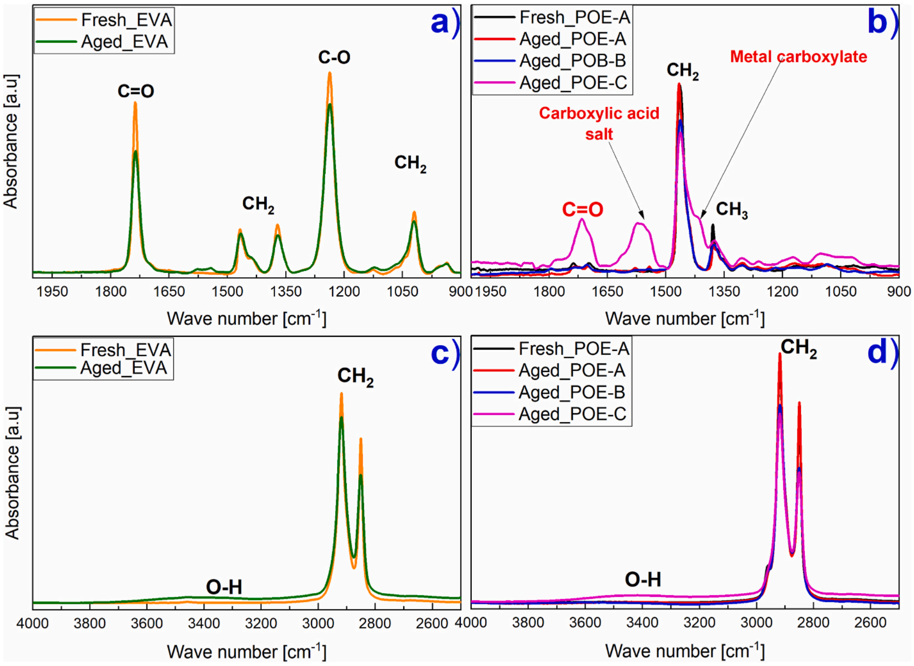

Fig. 5. ATR-FTIR zoomed in spectrum of a) 1950-900 cm^{-1} region of fresh and aged EVA, b) 1950-900 cm^{-1} region of fresh and aged POE highlight carboxylic formation/salt and metal carboxylate, c) O-H stretching region (4000-2600 cm^{-1}) of EVA and d) O-H stretching region (4000-2600 cm^{-1}) of POE to highlight the specific chemical change of the encapsulant that lead PV modules performance drop.

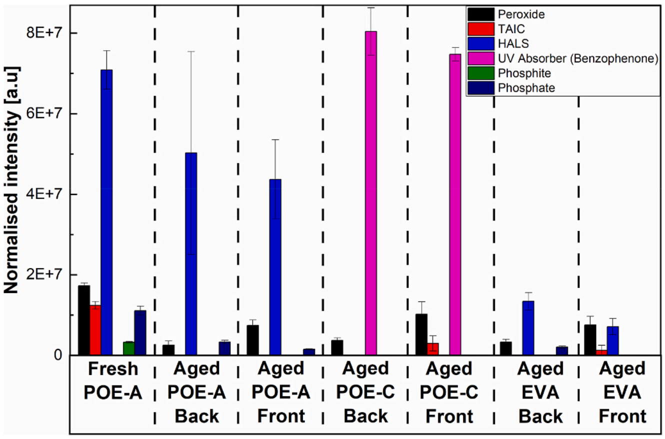

Fig. 6. Normalised Py-GC/MS additive profiles for fresh POE-A and damp-heat aged POE-A, POE-C, and EVA, highlighting six key additive classes: peroxide fragments (cross-linking initiators), triallyl isocyanurate (TAIC, a co-agent that enhances cross-link density and thermal stability), hindered-amine light stabilisers (HALS, self-regenerating radical scavengers that suppress UV-induced degradation), benzophenone UV absorbers (sacrificial UV shields), phosphites (secondary antioxidants that decompose hydroperoxides), and phosphates (stable oxidation products of phosphites indicating antioxidant activity during processing or ageing).

Py-GCMS indicates the absence of HALS and phosphite/phosphate antioxidants, with stabilisation relying primarily on a benzophenone UV absorber (sacrificial UV shields), an effective UV screen, but not a substitute for regenerative antioxidant systems. In polyolefins, HALS and phosphites act synergistically to quench radicals and decompose hydroperoxides; without them, thermo-oxidative autoxidation proceeds under damp-heat, likely yielding carbonyls and acidic end-groups [48–50]. The FTIR data (Figs. 4, 5b and 5d) are consistent with this pathway: growth of C=O/O–H features and new bands near ~1570 cm^{-1} (carboxylate, R–COO$^-$) and ~1440 cm^{-1} (metal carboxylate), assignments well-established for carboxylate/metal-carboxylate species [36–38,51]. Such acidic/carboxylate chemistry is likely involved in attacking cell metallisation and raising R_s, aligning with the observed ~400 % increase in R_s and a reduction in P_{max} of ~50 $\%_{rel}$. It is noted that although fresh POE-C could not be measured in this study, this does not materially affect the conclusion, as the absence of stabilisers and the degradation signatures observed in aged POE-C already provide a consistent mechanistic explanation.

It is also noted that Py-GCMS detected small residual peaks of the co-curing agent TAIC in the aged POE C front sample and in the aged EVA encapsulant. Py-GCMS is known to be highly sensitive to trace amounts of plastic additives and even residual crosslinking agents in crosslinked polymers, so the detection of such low-intensity signals does not, in itself, imply poor curing. The encapsulants were laminated within the usual processing window for peroxide-cured EVA/POE systems (peak temperatures ~145–155 °C, dwell times of several minutes), for which rheological and kinetic studies show that peroxyester and peroxyketal systems reach >90 % conversion within a few minutes [52–54]. Together with the datasheet gel contents (≈70–85 %), which fall in or above the range generally regarded as sufficiently cured for PV encapsulants, this suggests that the networks are overall well crosslinked. TAIC is a highly multifunctional co-agent that forms a crosslinked network already at relatively low overall conversion and whose polymerisation can become sterically and diffusion-limited, leaving a small fraction of unreacted allyl groups or co-agent molecules in the gel [55–57]. We therefore attribute the weak TAIC-derived peaks mainly to such residual, trapped species rather than to a globally low degree of cure. This interpretation is consistent with the near complete disappearance of peroxide-related peaks in all aged samples, in line with the use of residual peroxide enthalpy as a standard indicator of incomplete curing in EVA encapsulants [54].

In addition, it is also noted that peroxide-initiated crosslinking of EVA and POE encapsulants proceeds through free radicals generated by thermal decomposition of organic peroxides. These radicals can, however, also react with stabilisers present in the formulation. In peroxide-modified polyethylene and cross-linked polyethylene, some studies have shown that hindered phenolic antioxidants and other acidic aromatic stabilisers delay low-temperature pre-crosslinking and may slightly reduce the final crosslinking efficiency by competing for radicals [58, 59]. Similar interactions have been reported for EVA encapsulants containing benzophenone-type UV absorbers, where stabiliser-radical reactions can modify both curing and subsequent degradation behaviour [60]. In the materials studied here, Py-GCMS detects benzophenone-type UV absorbers, phosphite/phosphate stabilisers, and HALS in addition to the peroxide/TAIC curing system. These additives may therefore influence the detailed curing kinetics. Nevertheless, the combination of lamination conditions that lie within or slightly above the processing windows recommended for the POE grades where they are specified, the gel-content specifications (>70 % for POE-A, ≥75 % for POE-B, 55–85 % for POE-C, and ≥80 % for EVA; as detailed in Table 1), and the nearly complete disappearance of peroxide peaks in all aged samples shown in Fig. 6 indicates that the encapsulants as used here reach a high overall degree of cure.

3.3. *Solar cell metal contact failure analysis*

Fig. 7 presents the XPS survey spectra of the Ag contacts from various cells: a fresh cell that is non-encapsulated and has not undergone DH testing, as well as cells removed from aged EVA, POE-A, and POE-C encapsulations. The fresh cell exhibits distinct peaks corresponding to C 1s, O 1s, N 1s, Ag 3d, Si 2p, and Pb 4f. In contrast, the spectra from the aged cells extracted from EVA, POE-A, and POE-C encapsulated modules primarily show intense signals for C 1s, O 1s, and Ag 3d, while the Si 2p, Pb 4f, and N 1s signals are no longer detectable above the noise level.

Under the same acquisition conditions, the absence of Si and Pb signals, coupled with the strong intensities of C and O, suggests that the silver grid has become covered by a thicker layer of corrosion products and carbon-rich residues resulting from the encapsulant/flux system. Additionally, this indicates a depletion of lead from the glass frit. Consequently, we primarily utilise the survey spectra to confirm the overall elemental trends, specifically, the loss of substrate (Ag and Si) signals and the increase in surface carbon and oxygen. Detailed information about the chemical states is obtained from the high-resolution Ag 3d and C 1s spectra discussed in the following section.

Fig. 8 illustrates the C 1s core-level spectra of the Ag contact for the fresh cell and for cells removed from modules with EVA, POE-A, and POE-C. All spectra were referenced to the main hydrocarbon peak at 284.8 eV and fitted with conventional components. For the Ag contact of fresh cell, the C 1s line shape is described by a dominant C-C/C-H component at ~284.8 eV and a smaller C-O/C-O-C contribution near ~286 eV [61], consistent with a thin adventitious overlayer and requiring no separate high-binding-energy O-C=O component. The Ag contact of POE-A and POE-C samples show very similar behaviour: both spectra are dominated by the C-C/C-H component with a small C-O contribution around 286 eV [61], and no distinct peak at ~288.5–289 eV is resolved, indicating that any carboxylic/carboxylate carbon at these interfaces represents only a minor fraction of the total C signal and lies below the deconvolution limit on these rough, partially corroded contacts. In contrast, the EVA-aged contact exhibits a much more complex C 1s envelope, requiring three additional components beyond C-C/C-H: a C-O contribution at ~286 eV, a clear O–C=O contribution at ~288.7–289 eV, and a low-binding-energy component at ~283 eV assigned to C-Ag/carbidic carbon [61]. Together, these features demonstrate that carboxylic/carboxylate species and metal-bound carbon are significantly enriched at the Ag surface after damp-heat exposure in the EVA-encapsulated module.

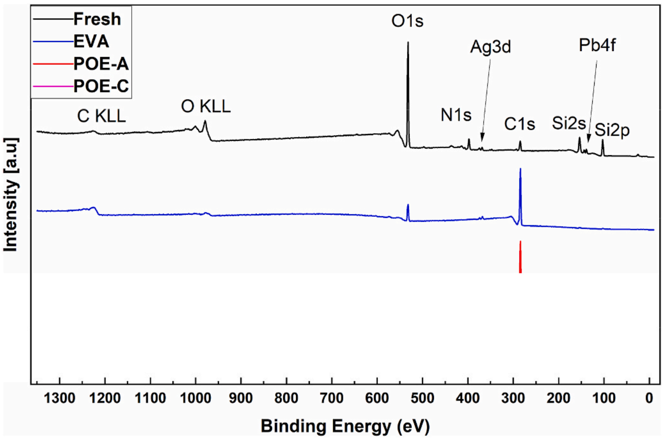

Fig. 7. XPS survey spectra for the Ag front contact in its fresh state, and after 1000 h of DH testing for cells encapsulated with EVA, POE-A, and POE-C.

Fig. 9 presents the evolution of XPS Ag 3d core-level spectra for the front Ag contact of fresh cell and cells removed from DH aged modules with POE-A, EVA and POE-C, respectively. The spectrum of the fresh Ag contact (a) shows a single, sharp Ag $3d_{5/2}$ peak centred at ~368.2 eV, characteristic of metallic silver (Ag^0) [61]. Its narrow full width at half maximum (FWHM) and the absence of any satellite features confirm a clean, unoxidised surface. The Ag spectrum from the POE-A encapsulated module (b) shows a comparatively milder degradation profile. The metallic Ag^0 peak at ~368.2 eV remains dominant (~60 %), accompanied by a weaker oxide/halide component at ~367.6 eV (~40 %). Notably, no Ag-carboxylate signal is detected, in agreement with FTIR results indicating that POE-A remains chemically stable and does not generate acidic species during ageing.

In contrast, the aged Ag contact from the EVA-encapsulated module (c) displays two distinct chemical states. A dominant peak at ~367.6 eV (~70 %) corresponds to oxidised silver species, such as Ag_2O or Ag-halides [61], indicating corrosion. A secondary component at ~368.8 eV (~30 %) is likely attributed to Ag-carboxylates (e.g., silver acetate), consistent with acetic acid release from EVA hydrolysis under heat and humidity [61]. The significant reduction in the metallic Ag^0 signal underscores the aggressive chemical environment created by EVA degradation.

In the case of POE-C (d), the Ag contact exhibits the most complex corrosion profile. The spectrum consists of three components: a dominant Ag_2O/Ag-halide peak at ~367.6 eV (~69 %), a high-binding-energy Ag-carboxylate signal at ~368.6 eV (~12 %), and a low-binding-energy feature at ~367.1 eV (~20 %), attributed to AgF_2, indicating fluoride-induced corrosion likely originating from residual flux [13,26]. The near-complete loss of the metallic Ag^0 signal reflects severe multi-path degradation of the silver contact. Overall, the XPS results reveal a progressive trend in corrosion severity, from a pristine metallic surface in the fresh sample, to mild oxidation in POE-A, to mixed oxidation and carboxylation in EVA, and finally to extensive carboxylate and fluoride attack in POE-C. This trend aligns well with the chemical signatures observed by FTIR and the corresponding power degradation observed in the modules.

It is important to note that XPS has been shown to be a powerful tool for analysing encapsulant degradation and interfacial chemistry in EVA and POE systems [62]. In the present work, however, we did not perform XPS on free-standing EVA/POE films for two main reasons. First, severe charging and adventitious contamination on thick, highly insulating polymer films make the absolute surface composition difficult to interpret quantitatively. Second, the bulk chemical evolution of the encapsulants is already captured more robustly by ATR-FTIR and Py-GCMS (Figs. 4–6), which clearly reveal ester hydrolysis and acetic-acid formation in EVA and the emergence of carboxylic/metal-carboxylate species in POE-C, but not in POE-A/POE-B. In addition, no pristine (unlaminated) EVA, POE-B or POE-C films were available for XPS in this study. The only accessible encapsulant material was recovered from damp-heat-aged industrial modules, and these fragments were extremely small, irregularly shaped and lacked the flat surface area (≈1 cm × 1 cm with minimal curvature) required for reliable measurements at the UNSW XPS facility. This limitation arises from the delamination of

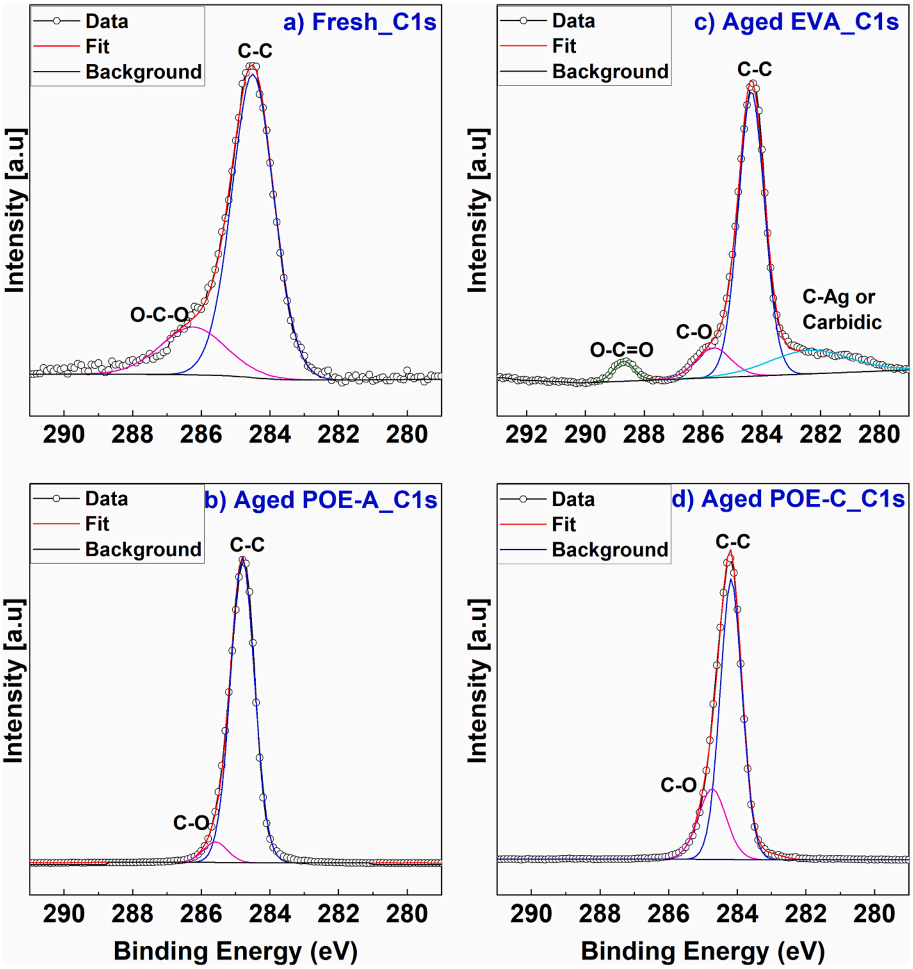

Fig. 8. XPS C 1s core-level spectra for the Ag front contact: (a) in its fresh state, and after 1000 h of DH testing for cells encapsulated with (b) EVA, (c) POE-A, and (d) POE-C.

tempered-glass laminates, where both glass and encapsulant fracture into many small pieces that are difficult to separate while preserving surface flatness. Consequently, XPS measurements in this study were focused on the Ag front contacts of the cells.

Figs. 10 and 11 present cross-sectional SEM images and corresponding SEM-EDS elemental maps of front Ag contacts from fresh and aged cells removed from modules with POE-A, EVA, and POE-C, respectively. The fresh contacts, shown in Fig. 10(a and b) and 11(a), display a dense, well-sintered Ag microstructure with uniform distribution, indicative of a continuous and conductive network. The contact remains firmly bonded to the underlying Si surface, with minimal porosity or void formation. Elemental mapping confirms that Pb and O is primarily localised within the glass frit phase, while Al is also confined to the glass frit. Lead oxide (PbO) appears predominantly at the Ag/glass interface, often surrounding the spherical Al-rich domains, consistent with typical glass frit formulations. No signs of corrosion or structural deterioration are observed.

The front contact from a cell removed from a POE-A encapsulated module (Fig. 10c and 11b) shows a microstructure and composition nearly identical to the fresh reference. The Ag remains compact and continuous, with no signs of significant void formation. The Al particles retain their nearly spherical morphology, and the distribution and intensity of O and Pb are similar to those of the fresh sample, indicating that POE-A effectively preserves the contact integrity under DH conditions.

Similarly, the front contact from a cell removed from an EVA-encapsulated module (Fig. 10d and 11c) shows a well-preserved microstructure. The Ag matrix remains intact, and no microcracks or porosity are detected. The Al particle shape remains relatively unchanged, and the O signal distribution aligns with those of the fresh and POE-A samples. However, a slight reduction in Pb intensity is observed around the Al-rich regions, suggesting potential leaching or reaction of PbO. This may be attributed to the presence of acetic acid released from EVA hydrolysis and organic acids from soldering flux residues, which could chemically react with PbO in the glass frit and facilitate its dissolution [13].

In contrast, the contacts from cells encapsulated with POE-C (Fig. 10e and f and 11d–e) exhibit extensive microstructural degradation. The Ag contact is highly porous and fragmented, with widespread cracking, voids, and structural collapse. The EDS maps show a pronounced increase in oxygen content, particularly in areas surrounding Al, indicating extensive oxidation. The Al signal is concentrated in degraded regions, suggesting the presence of hydrolysis-driven reactions involving Al-containing additives. Pb is significantly depleted throughout the contact, consistent with acid-driven leaching.

4. Discussion

4.1. Potential corrosion pathway

Based on comprehensive analytical evidence from I-V, EL, FTIR, Py-GCMS, XPS and SEM-EDS, it is likely that the module with POE-C underwent a complex degradation mechanism, resulting in a substantial increase in R_s and a severe reduction in P_{max}. This failure was not likely

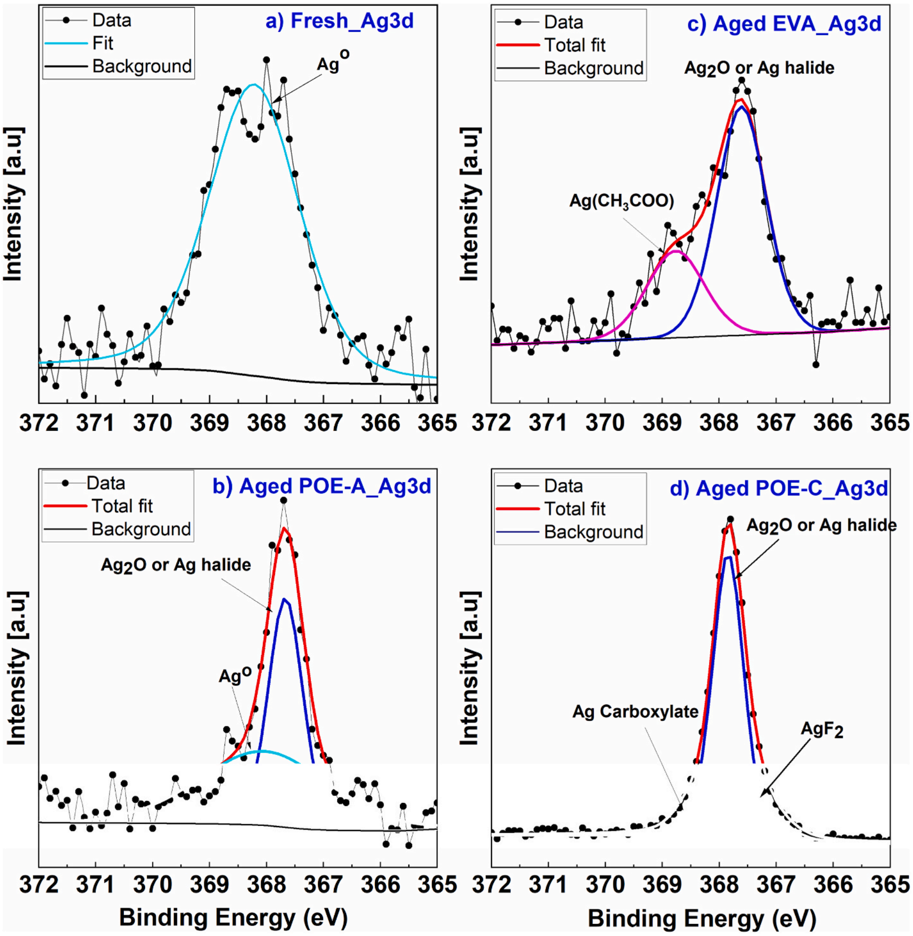

Fig. 9. XPS Ag 3d core-level spectra for the Ag front contact: (a) in its fresh state, and after 1000 h of DH testing for cells encapsulated with (b) EVA, (c) POE-A, and (d) POE-C.

driven by a single mechanism but by a cascade of interacting chemical and electrochemical processes, initiated by the formation of a potent acidic environment within the laminate. The damp heat test conditions (85 °C, 85 % RH) likely activated three distinct but synergistic sources of organic acids that collectively lowered the pH at metal-polymer interfaces:

Pathway 1: Thermo-oxidative degradation of POE: Although POE is marketed as “acid-free” because it lacks vinyl acetate (the acetic-acid precursor in EVA), its polyethylene backbone remains susceptible to thermo-oxidative degradation [18,19,63–65]. Py-GCMS (Fig. 6) shows no detectable HALS and no phosphite/phosphate antioxidants, indicating poor long-term stabilisation [49,66]. In PE-based encapsulants, HALS are the primary, durable defence: they intercept alkyl and peroxy radicals (R•, ROO•) and regenerate catalytically, whereas phosphites mainly provide short-term hydroperoxide control. Without HALS, exposure to heat, oxygen, and moisture allows free-radical autoxidation to proceed, generating R• → ROO• → ROOH and, upon ROOH decomposition, ketones, aldehydes, and, critically, carboxylic acids (R–COOH) [67]. This mechanism is consistent with the observed FTIR growth of carbonyl bands ($\sim$1710–1740 cm^{-1}), a standard marker of oxidation in polyolefins.

Pathway 2: Residual soldering flux: Soldering fluxes used at interconnects/busbars commonly employ weak organic acids (WOAs), often dicarboxylic acids [68,69] such as azelaic acid, as also detected in our previous work (Flux A) [13,26], as activators; if not fully removed, residues can remain at the joints and within the laminate. Under heat and humidity, these WOA residues are hygroscopic/reactivate, forming localised acidic micro-environments that drive metal corrosion and series-resistance growth [13,26,68]. Initially concentrated at interconnects, as demonstrated in our previous work [3], the acid attack likely propagated over time across broader areas of the cell surface.

Pathway 3: Decomposition of benzophenone UV absorber: Py-GCMS (Fig. 6) identifies a benzophenone-type UV absorber as a major additive in the POE. Although such absorbers are intended to work reversibly, they can undergo secondary degradation in oxidative microenvironments, yielding lower-molecular-weight acids and phenolics. Previous studies have shown that benzophenone-based UV absorbers react with radicals, leading to undesired side reactions [60,70]. Based on the general thermo-oxidative aging of PE and the carbonyl groups detected in the FTIR measurements, which confirm this form of aging [71,72], PE can potentially generate ultra-short-living hydroxyl radicals (a), short-living alkoxy radicals (b) and long-living peroxyl radicals (c) during degradation [71,73]. Fig. 12 displays a simplified degradation scheme of PE with possible pathways for the generation of Hydroperoxides and their decomposition in the three radical species.

Hydroxyl radicals react very quickly with their environment [73], so their influence on the initial reaction of the benzophenone-based UV absorber can probably be neglected, unless the hydroxyl group of the UV absorber is in the immediate vicinity. Fig. 13 shows a potential attack by alkoxy or peroxyl radicals on the UV absorber. Here, R_3 is the OC_8H_{17} rest group. According to the work of Gong et al., hydrogen abstraction at the hydroxyl group of benzophenone by radical attacks could potentially lead to the splitting into two aryl groups [74]. From this point, it is conceivable that the two fragments could react further. On the one hand, hydrogen abstraction from surrounding polymer chains can quickly lead to the formation of a phenol group. On the other hand, reaction with free

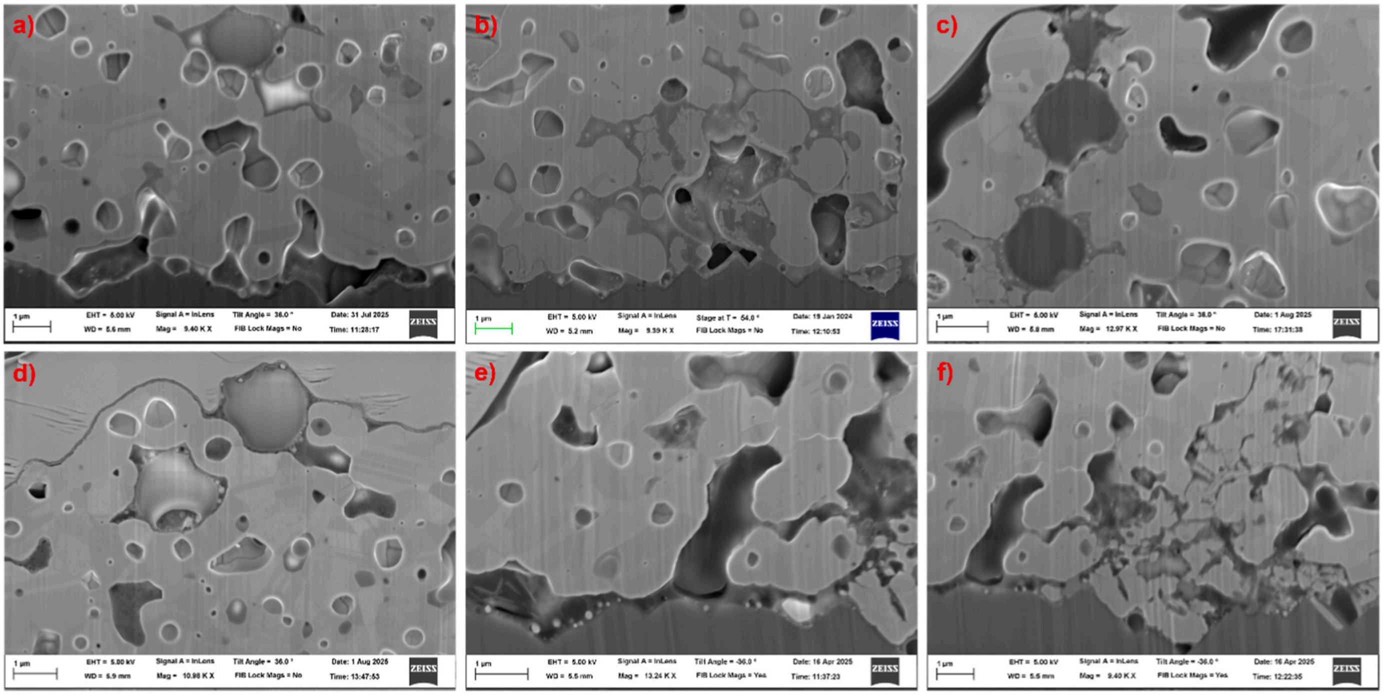

Fig. 10. Cross-sectional SEM images of front Ag metal contacts: (a) and (b) show well-sintered, undamaged fresh contacts; (c) shows the contact from a cell encapsulated with POE-A; (d) shows the contact from a cell encapsulated with EVA; and (e) and (f) show severely degraded contacts from cells encapsulated with POE-C.

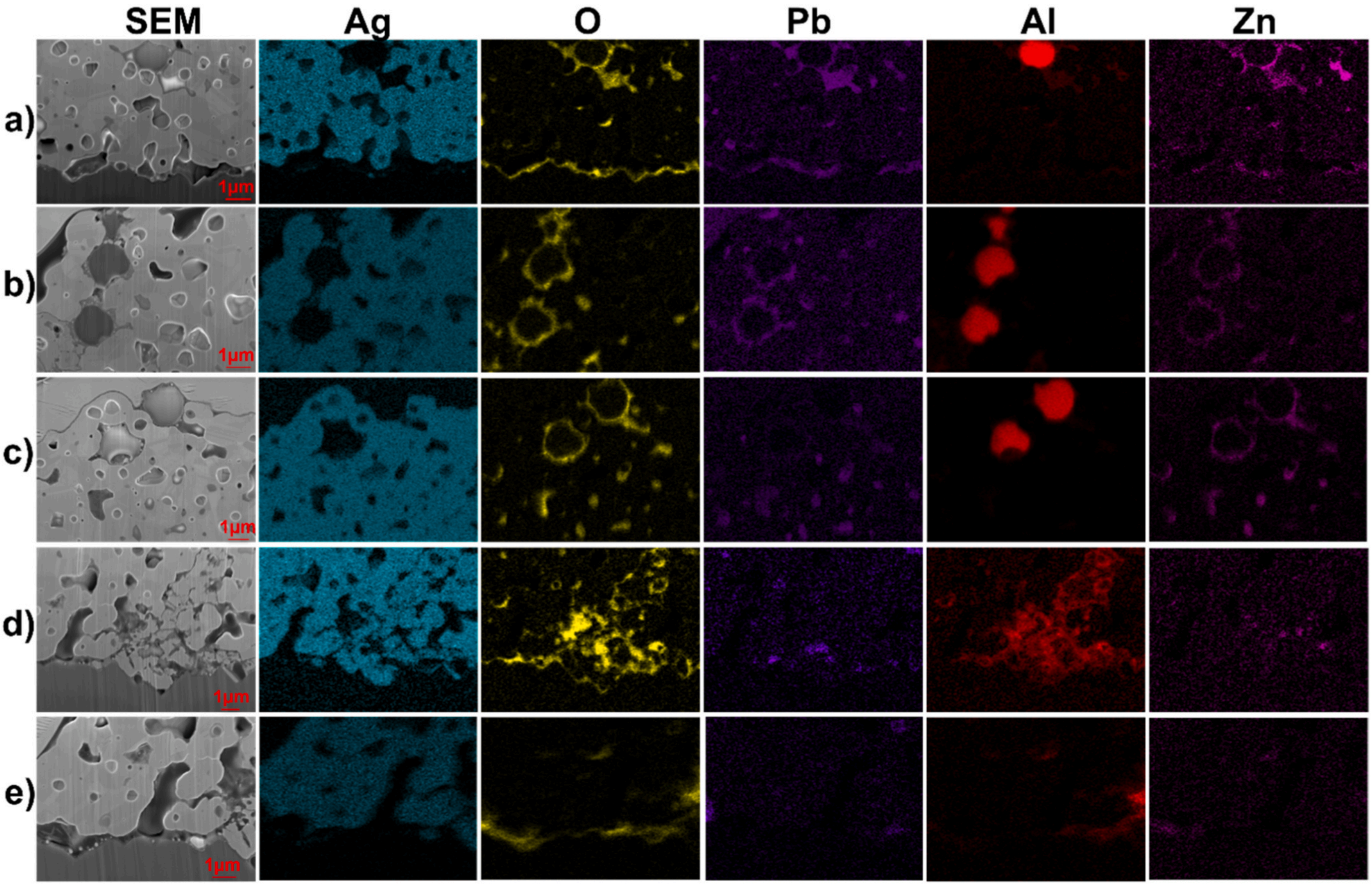

Fig. 11. Cross-sectional SEM-EDS elemental maps of front Ag contacts: (a) fresh contact with uniform elemental distribution; (b) contact from a cell encapsulated with POE-A; (c) from a cell with EVA; and (d–e) from cells encapsulated with POE-C, showing increased oxidation and elemental redistribution.

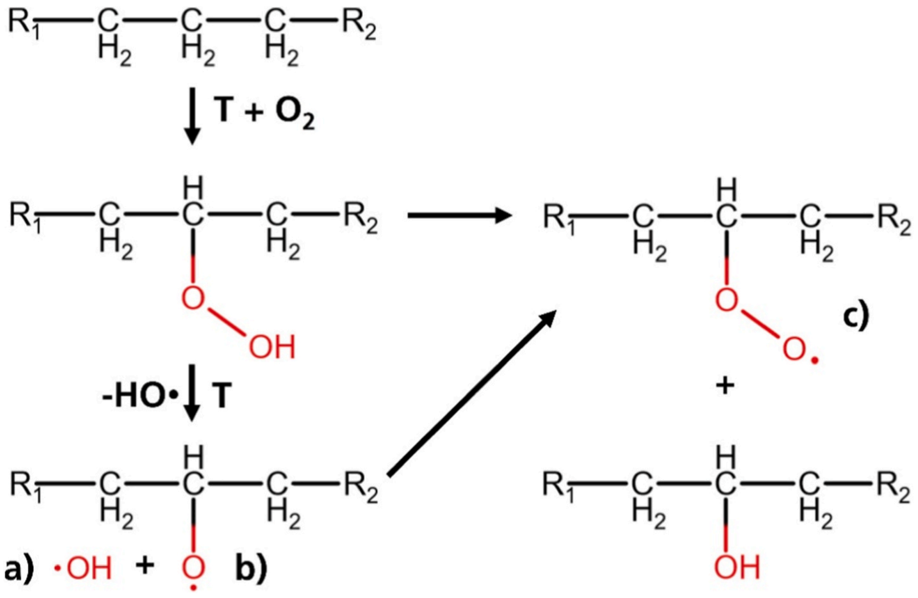

Fig. 12. Simplified degradation scheme of polyethylene showing hydroperoxide formation and its subsequent decomposition into three radical species: (a) hydroxyl radical (·OH) and alkoxy radical (·O·), (b) alkoxy radical (·O·), and (c) peroxy radical (ROO·) with a secondary alcohol.

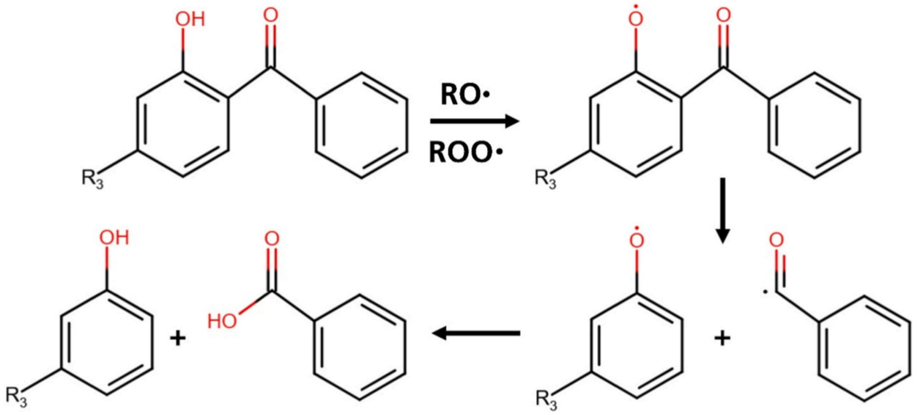

Fig. 13. Potential degradation pathway of the UV absorber initiated by alkoxy (RO·) or peroxyl (ROO·) radicals. The radical attack leads to cleavage and formation of phenoxy and benzoyl radical intermediates, ultimately yielding hydroxylated products. Here, R_3 represents the OC_8H_{17} substituent.

hydroxyl radicals could lead to the formation of benzoic acid. The latter reaction would explain the acidic environment that led to the observed corrosion effects. However, the exact mechanism has yet to be proven.

The combination of these three pathways likely created a highly aggressive chemical environment a corrosive mixture of aliphatic and aromatic carboxylic acids, that far exceeded the corrosive potential of any individual source. This synergistic acid generation likely underpinned the subsequent electrochemical corrosion processes that ultimately led to catastrophic mini-module failure.

4.2. Electrochemical corrosion of metallisation: the cascade of failure

Following the formation of a highly acidic and moist internal environment, driven by degradation of the POE encapsulant, residual soldering flux, and benzophenone UV absorber, the module's metal contacts were likely exposed to a corrosive electrolyte. This set the stage for a cascade of electrochemical corrosion reactions that ultimately compromised the front-side metallisation.

4.2.1. Acid-Mediated corrosion and passivation breakdown

The front grid consisted predominantly of Ag. Prior to the introduction of laser-assisted firing, a controlled amount of Al was deliberately included in many Ag pastes (especially for n-type/B-emitter and TOPCon contacting) to lower contact resistivity during firing by promoting the formation of conductive Ag-Al “spikes”/crystallites that penetrate the dielectric/ARC and establish ohmic contact to Si. This Al-assisted spiking is effective for contact resistivity (R_c) reduction but also introduces corrosion vulnerability at the contact interface [14,15,75]. Al is highly reactive in aqueous environments but is usually protected by a nanometric passive Al_2O_3 film [76–78]. This oxide is only stable in a near-neutral window (≈pH 4–8.5). Acidic conditions dissolve the passive layer, exposing bare Al. Once the local pH drops below this range, e.g., due to organic acids (R–COOH) generated within the laminate, the passive film can be removed according to:

$$Al_2O_3+6H^+ \rightarrow 2Al^{3+} +3H_2O$$

Once exposed, Al corroded rapidly. The resulting Al^{3+} ions likely reacted with carboxylate anions (R–COO$^-$) to form insulating aluminum carboxylate salts, such as aluminum benzoate [79], further increasing R_s:

$$Al^{3+}+3R-COO^- \rightarrow Al(R-COO)_3$$

Moreover, the commercial front-side Ag pastes typically contain a PbO-borosilicate glass frit, often with ZnO modifiers. As shown in cross-sectional SEM–EDS (Fig. 11), the Pb map/intensity drops markedly after ageing a particular contact of the cell removed from the module with POE-C and EVA. Because the primary Pb reservoir is PbO in the frit, a loss of Pb at the interface is consistent with acid-assisted glass depolymerisation and subsequent conversion or migration of Pb^{2+}. A plausible sequence is:

- Proton-driven attack on the frit network liberates Pb^{2+} from Pb–O–Si linkages (general silicate-glass corrosion pathway [80].
- In the presence of weak organic acids (R–COOH) present in the laminate (e.g., benzoic or dicarboxylic acids from additives/flux residues and/or acid from POE additive and/or acetic acid from EVA), Pb^{2+} is likely converted to poorly conductive lead carboxylates that can redistribute or be partially removed during specimen preparation [81,82]:

$$\mathrm{PbO\ (glass)} + 2\ \mathrm{RCOOH} \rightarrow \mathrm{Pb\ (RCOO)_2} + \mathrm{H_2O}$$

$$\mathrm{Pb^{2+}} + 2\ \mathrm{RCOO^-} \rightarrow \mathrm{Pb\ (RCOO)_2}$$

This explains the reduced Pb signal adjacent to the Ag contact, while occasional Pb-rich speckles or clusters appear in voided or cracked regions. In cells removed from both EVA- and POE-C-laminated modules (Fig. 11c–e), hydrolysis generates acetic acid from EVA and other carboxylic acids from POE-C, which more aggressively depolymerise the PbO-borosilicate frit. This releases Pb^{2+} ions that can (i) migrate and re-precipitate as lead carboxylates away from the interface or (ii) re-oxidise to PbO during drying, ageing, or local e-beam heating. These processes lead to Pb depletion at the immediate contact and discrete PbO-rich islands nearby, matching the contrast seen between fresh (Fig. 11a) and aged EVA (Fig. 11c) and POE-C (Fig. 11d and e) maps. The loss of Pb from the glass matrix undermines glass-Ag cohesion, reduces frit softening/reflow, and produces electronically poor corrosion products, effects that collectively increase R_s. Where Zn-bearing modifiers are present, analogous zinc carboxylates may form, further diminishing electronic connectivity.

4.2.2. *Galvanic corrosion: a synergistic amplifier*

The front-side contact stack (Ag grid with Al- and Pb-containing glass frit, Zn from the paste) constitutes an electrically continuous couple of dissimilar metals. In an acidic, humid electrolyte, this configuration behaves as a galvanic cell: the more noble Ag acts predominantly as the cathode, while Al and Zn, far more active in the galvanic series, become local anodes and dissolve preferentially [83,84].

This electrochemical arrangement creates a potent corrosion cell. The large surface area of the silver grid facilitates cathodic reactions, primarily the reduction of hydrogen ions and dissolved oxygen [85]:

$$2\mathrm{H^+} + 2\mathrm{e^-} \rightarrow \mathrm{H_2\ (gas)}$$

$$\mathrm{O_2} + 4\mathrm{H^+} + 4\mathrm{e^-} \rightarrow 2\mathrm{H_2O}$$

These reactions draw electrons from the less noble metals, driving the accelerated and preferential oxidation (corrosion) of aluminium and zinc:

$$\mathrm{Al} \rightarrow \mathrm{Al^{3+}} + 3\mathrm{e^-}$$

$$\mathrm{Zn} \rightarrow \mathrm{Zn^{2+}} + 2\mathrm{e^-}$$

Consequently, these anodic regions corrode far more rapidly than they would through acid attack alone. This conclusion is strongly supported by the SEM-EDS analysis of metal contact of cells removed from the module with POE-C (Fig. 10e and f, 11d-e), which reveals pronounced structural degradation specifically in the aluminum-rich regions of the contact, providing clear evidence of galvanic acceleration.

4.2.3. *Formation of secondary corrosion products: Ag_2O and AgF*

Further analysis by XPS on the metal contact of cells removed from the module with POE-C (Fig. 9d) confirmed the formation of two key secondary degradation products on the silver grid: Ag_2O and AgF. The presence of Ag_2O indicates that the silver grid itself underwent direct oxidation, a process catalysed by the acidic and humid environment:

$$2\mathrm{Ag} + \mathrm{H_2O} \rightarrow \mathrm{Ag_2O} + 2\mathrm{H^+} + 2\mathrm{e^-}$$

The detection of AgF points to a corrosion mechanism involving fluorine, likely originating from the soldering flux [11,26]. As shown in our previous work [11,26], modern flux formulations may contain thermally decomposable fluorinated compounds (e.g., fluorocarbons, fluoroborates). Under heat and humidity, these degrade to release hydrofluoric acid (HF):

$$\text{Fluorinated compound} + \text{Heat}/\mathrm{H_2O} \rightarrow \mathrm{HF} + \text{byproducts}$$

This HF readily attacks the silver metallisation, particularly the newly formed silver oxide, to produce silver fluoride, a poorly conductive salt that further degrades the contact and increases series resistance:

$$\mathrm{Ag_2O} + 2\mathrm{HF} \rightarrow 2\mathrm{AgF} + \mathrm{H_2O}$$

The formation of both these oxide and fluoride layers contributes significantly to the observed increase in R_s and the overall degradation of the module's performance.

Collectively, the data are consistent with a mechanistic pathway in which acid formation initiates corrosion, galvanic coupling intensifies it, and secondary reactions further accelerate it, progressively compromising the front-side current-collection network, as reflected by the marked rise in R_s and the widespread microstructural damage observed across techniques (Table 2).

5. Conclusion

This study investigates corrosion-induced degradation in TOPCon minimodules encapsulated with EVA and three commercially sourced polyolefin elastomers (POE-A, POE-B, and POE-C) under damp-heat conditions (85 °C, 85 % RH for 1000 h). The EVA encapsulated module exhibited a ~11 $\%_{rel}$ reduction in P_{max}, primarily driven by a 50 % increase in R_s. Spectroscopic analysis indicates that acetic acid released from EVA hydrolysis reacts with solder flux residues, promoting corrosion at the front metallisation. In contrast, POE-A and POE-B modules showed significantly lower degradation (6–10 $\%_{rel}$) and did not produce measurable organic acids. In particular, POE-A benefited from the presence of antioxidants that suppressed polymer oxidation; residual power loss was likely attributed to pre-lamination contamination. However, POE-C modules suffered a drastic 55 $\%_{rel}$ drop in P_{max}, accompanied by a severe rise in R_s. Multi-technique analysis (I–V, EL, FTIR, Py-GCMS, XPS, SEM-EDS) suggest a potential cascade of mutually reinforcing degradation pathways: (i) thermo-oxidative degradation of

Table 2
Summary of key potential electrochemical and chemical corrosion reactions.

Process	Potential Reaction
Acid Formation	$\mathrm{R{-}CH_2{-}R'} + \mathrm{O_2} + \mathrm{Heat/H_2O} \rightarrow \mathrm{R{-}COOH}$ (from POE) $\mathrm{(C_6H_5)_2CO} + \mathrm{Heat/H_2O} \rightarrow \mathrm{C_6H_5COOH}$ (from benzophenone) Azelaic acid, fluorinated residues (from flux)
Anodic Reactions	$\mathrm{Al} \rightarrow \mathrm{Al^{3+}} + 3\mathrm{e^-}$; $\mathrm{Zn} \rightarrow \mathrm{Zn^{2+}} + 2\mathrm{e^-}$; $\mathrm{Pb} \rightarrow \mathrm{Pb^{2+}} + 2\mathrm{e^-}$; $\mathrm{Ag} \rightarrow \mathrm{Ag^+} + \mathrm{e^-}$
Cathodic Reactions	$2\mathrm{H^+} + 2\mathrm{e^-} \rightarrow \mathrm{H_2}$; $\mathrm{O_2} + 4\mathrm{H^+} + 4\mathrm{e^-} \rightarrow 2\mathrm{H_2O}$
Acid Attack & Salt Formation	$\mathrm{Al_2O_3} + 6\mathrm{H^+} \rightarrow 2\mathrm{Al^{3+}} + 3\mathrm{H_2O}$ $\mathrm{Al^{3+}} + 3\mathrm{R{-}COO^-} \rightarrow \mathrm{Al(R{-}COO)_3}$; $\mathrm{Pb} + 2\mathrm{R{-}COOH} \rightarrow \mathrm{Pb(R{-}COO)_2} + \mathrm{H_2}$ $\mathrm{Ag^+} + \mathrm{R{-}COO^-} \rightarrow \mathrm{Ag(R{-}COO)}$
Secondary Reactions	$2\mathrm{Ag} + \mathrm{H_2O} \rightarrow \mathrm{Ag_2O} + 2\mathrm{H^+} + 2\mathrm{e^-}$; $\mathrm{Ag_2O} + 2\mathrm{HF} \rightarrow 2\mathrm{AgF} + \mathrm{H_2O}$

the POE matrix, producing carboxylic acids; (ii) retained azelaic acid from soldering flux; and (iii) hydrolytic breakdown of benzophenone UV absorbers into benzoic and phenolic acids. Together, these compounds likely created an aggressive acidic environment that accelerated electrochemical corrosion of the front metal contact of TOPCon solar cells, ultimately resulting in catastrophic module failure. These findings highlight that the long-term field reliability of TOPCon modules depends critically on encapsulant formulation—particularly the choice of antioxidants and UV stabilisers—together with stringent control of flux residues, manufacturing cleanliness, and the intrinsic sensitivity of the solar cell.

CRediT authorship contribution statement

Chandany Sen: Writing – review & editing, Writing – original draft, Validation, Methodology, Investigation, Funding acquisition, Formal analysis, Data curation, Conceptualization. **Haoran Wang:** Methodology, Investigation, Data curation. **Robert Heidrich:** Writing – review & editing, Data curation, Conceptualization. **Marius Lüdemann:** Methodology, Investigation, Data curation. **Muhammad Umair Khan:** Methodology, Investigation, Data curation. **Bram Hoex:** Writing – review & editing, Supervision, Resources, Project administration, Funding acquisition, Conceptualization.

Declaration of competing interest

☑ The authors declare that they have no known competing financial interests or personal relationships that could have appeared to influence the work reported in this paper.

Acknowledgment

The authors gratefully acknowledge the support of the Australian Government's Trailblazer for Recycling and Clean Energy (TRaCE) program, led by UNSW and the University of Newcastle. Additional support was provided by the Australian Centre for Advanced Photovoltaics (ACAP), funded by the Australian Renewable Energy Agency (ARENA). The views, information, and advice expressed herein are those of the authors and do not necessarily reflect those of the Australian Government. The authors also acknowledge the use of key instrumentation, including XPS at the Surface Analysis Laboratory, FTIR at the Spectroscopy Laboratory, and CryoFIB-SEM at the UNSW Mark Wainwright Analytical Centre. Special thanks are extended to the SLDOT team at SPREE UNSW, both at the TETB and SIRF facilities, for their critical support in maintaining high health and safety standards and ensuring smooth operation of the laboratory infrastructure, which enabled the successful execution of this work.

Data availability

Data will be made available on request.

References

[1] I.M. Peters, J. Hauch, C. Brabec, P. Sinha, The value of stability in photovoltaics, Joule 5 (2021) 3137–3153, https://doi.org/10.1016/j.joule.2021.10.019.

[2] V.D.M.A. Photovoltaics Equipment, International Technology Roadmap for Photovoltaics (ITRPV): Results, sixteenth ed., 2024. VDMA, 2025.

[3] C. Sen, H. Wang, M.U. Khan, J. Fu, X. Wu, X. Wang, B. Hoex, Buyer aware: three new failure modes in TOPCon modules absent from PERC technology, Sol. Energy Mater. Sol. Cell. 272 (2024), https://doi.org/10.1016/j.solmat.2024.112877.

[4] C. Sen, H. Wang, M.U. Khan, J. Yang, Z. Zhu, A. Li, B. Hoex, Hidden traces: insights into how solar cell handling drives damp-heat failures in HJT and TOPCon modules, Sol. Energy Mater. Sol. Cell. 289 (2025), https://doi.org/10.1016/j.solmat.2025.113695.

[5] X. Wu, X. Wang, R. Lv, H. Song, Y. Yu, C. Sen, Y. Cheng, M.U. Khan, A. Ciesla, T. Xu, G. Zhang, B. Hoex, Unveiling the degradation mechanisms in silicon heterojunction solar cells under accelerated damp-heat testing, Sol. Energy Mater. Sol. Cell. 282 (2025), https://doi.org/10.1016/j.solmat.2024.113325.

[6] P. Gebhardt, U. Kräling, E. Fokuhl, I. Hädrich, D. Philipp, Reliability of commercial TOPCon PV Modules—An extensive comparative Study, Prog. Photovoltaics Res. Appl. (2024), https://doi.org/10.1002/pip.3868.

[7] P. Gebhardt, S. Marletti, J. Markert, U. Kraling, M. Tu, I. Haedrich, D. Philipp, Comparison of commercial TOPCon PV modules in accelerated aging tests, IEEE J. Photovoltaics (2024), https://doi.org/10.1109/JPHOTOV.2024.3483317.

[8] Z. Li, J. Tang, K. Yu, Q. Xiao, Q. Zhu, X.J. Li, Z. Ji, B. Huang, J. Huang, L. Wang, Y. Chen, X. Sun, J. Gao, L. Zhou, Effect of firing temperature on damp heat stability of n-TOPCon solar cells' rear side, Sol. RRL 9 (2025), https://doi.org/10.1002/solr.202500299.

[9] P.M. Sommeling, J. Liu, J.M. Kroon, Corrosion effects in bifacial crystalline silicon PV modules; interactions between metallization and encapsulation, Sol. Energy Mater. Sol. Cell. 256 (2023), https://doi.org/10.1016/j.solmat.2023.112321.

[10] Y. Ye, Y. Zhou, Y. Wang, B. Hoex, X. Zhu, D. Chen, W. Xue, T. Wei, B. Chen, M. Cheng, J. Lu, H. Yin, Z. Ouyang, Damp-heat stability investigation of glass-backsheet modules based on TOPCon solar cells, Sol. Energy Mater. Sol. Cell. 292 (2025), https://doi.org/10.1016/j.solmat.2025.113764.

[11] C. Sen, X. Wu, H. Wang, M.U. Khan, L. Mao, F. Jiang, T. Xu, G. Zhang, C. Chan, B. Hoex, Accelerated damp-heat testing at the cell-level of bifacial silicon HJT, PERC and TOPCon solar cells using sodium chloride, Sol. Energy Mater. Sol. Cell. 262 (2023) 112554, https://doi.org/10.1016/j.solmat.2023.112554.

[12] X. Wu, C. Sen, X. Wang, Y. Cheng, R. Lv, H. Song, Y. Yu, B. Liao, S. Ma, M.U. Khan, A. Ciesla, B. Hoex, Unveiling the origin of metal contact failures in TOPCon solar cells through accelerated damp-heat testing, Sol. Energy Mater. Sol. Cell. 278 (2024), https://doi.org/10.1016/j.solmat.2024.113188.

[13] J. Fu, C. Sen, H. Wang, M.U. Khan, H. Song, R. Lv, T. Huang, B. Hoex, Assessing the impact of solder flux-induced corrosion on TOPCon solar cells, Sol. Energy Mater. Sol. Cell. 294 (2026) 113890, https://doi.org/10.1016/j.solmat.2025.113890.

[14] G. Xing, W. Chen, Y. Liu, X. Du, Regulation to Ag–Al spikes through silver aluminum paste with Al–Si alloy, Sol. Energy Mater. Sol. Cell. 273 (2024), https://doi.org/10.1016/j.solmat.2024.112968.

[15] W. Wu, K.E. Roelofs, S. Subramoney, K. Lloyd, L. Zhang, Role of aluminum in silver paste contact to boron-doped silicon emitters, AIP Adv. 7 (2017), https://doi.org/10.1063/1.4974752.

[16] X. Wu, X. Wang, W. Yang, J. Nie, J. Yuan, M.U. Khan, A. Ciesla, C. Sen, Z. Qiao, B. Hoex, Enhancing the reliability of TOPCon technology by laser-enhanced contact firing, Sol. Energy Mater. Sol. Cell. 271 (2024), https://doi.org/10.1016/j.solmat.2024.112846.

[17] Eitner Ulrich, Sarah Kajari-Schröder, Mechanical properties of EVA-based encapsulants, Photovoltaics International (PV-Tech Technical Paper, PV Modules Section) 12 (2011) 156–160. www.otto-solar.com.

[18] C. Barretta, G. Oreski, S. Feldbacher, K. Resch-Fauster, R. Pantani, Comparison of degradation behavior of newly developed encapsulation materials for photovoltaic applications under different artificial ageing tests, Polymers 13 (2021) 1–21, https://doi.org/10.3390/polym13020271.

[19] D.E. Mansour, C. Barretta, L.P. Bauermann, G. Oreski, A. Schueler, D. Philipp, P. Gebhardt, Effect of backsheet properties on PV encapsulant degradation during combined accelerated aging tests, Sustainability 12 (2020), https://doi.org/10.3390/su12125208.

[20] E.C. Palmiotti, C.C. Roberts, B.H. King, Thermal behaviors of ethylene vinyl acetate encapsulants in fielded silicon photovoltaic modules, J. Appl. Polym. Sci. 140 (2023), https://doi.org/10.1002/app.54337.

[21] G. Oreski, A. Omazic, G.C. Eder, Y. Voronko, L. Neumaier, W. Mühleisen, C. Hirschl, G. Ujvari, R. Ebner, M. Edler, Properties and degradation behaviour of polyolefin encapsulants for photovoltaic modules, Prog. Photovoltaics Res. Appl. 28 (2020) 1277–1288, https://doi.org/10.1002/pip.3323.

[22] Y. Bai, Y. Zhao, J. Li, H. Chen, A. Lambertz, Q. Qiu, C. Qian, J. Shi, W. Liu, T. Chen, J. Yu, K. Ding, J. Yu, Lower levelized cost of energy achievement of silicon heterojunction solar modules with low water vapor transmission rate encapsulants, Energy Technol. 11 (2023), https://doi.org/10.1002/ente.202201466.

[23] JinkoSolar: transparent backsheet vs dual glass—Advantages and disadvantages, PV tech. https://www.pv-tech.org/industry-updates/jinkosolar-transparent-backsheet-vs-dual-glass-advantages-and-disadvantages/, 2020. (Accessed 18 July 2023).

[24] J.I., N.D.E., M.J.R., R.N.W., S.J.H.J., J.D.C. Goldstein, Scanning Electron Microscopy and X-ray Microanalysis, springer, 2017.

[25] R. Heidrich, A. Mordvinkin, R. Gottschalg, Quantification of UV protecting additives in ethylene-vinyl acetate copolymer encapsulants for photovoltaic modules with pyrolysis-gas chromatography-mass spectrometry, Polym. Test. 118 (2023), https://doi.org/10.1016/j.polymertesting.2022.107913.

[26] H. Wang, C. Sen, J. Fu, M.U. Khan, H. Song, R. Lv, G. Conibeer, B. Hoex, The influence of soldering flux on stability of heterojunction and TOPCon solar cells, Prog. Photovoltaics Res. Appl. (2025), https://doi.org/10.1002/pip.3896.

[27] C. Sen, H. Wang, X. Wu, M.U. Khan, C. Chan, M. Abbott, B. Hoex, Four failure modes in silicon heterojunction glass-backsheet modules, Sol. Energy Mater. Sol. Cell. 257 (2023) 112358, https://doi.org/10.1016/j.solmat.2023.112358.

[28] I. Zafirovska, M.K. Juhl, J.W. Weber, J. Wong, T. Trupke, Detection of finger interruptions in silicon solar cells using line scan photoluminescence imaging, IEEE J. Photovoltaics 7 (2017) 1496–1502, https://doi.org/10.1109/JPHOTOV.2017.2732220.

[29] M.A. Zahid, H. Yousuf, M. de Assis Rabelo, S.B. Cho, Y.W. Yang, E.C. Cho, J. Yi, Analysis of accelerated damp heat Test for degradation analysis and recovery method of Photovoltaic module, Energy Technol. 10 (2022), https://doi.org/10.1002/ente.202200707.

[30] Barbara H. Stuart, Infrared Spectroscopy: Fundamentals and Applications, John Wiley & Sons, Ltd., Chichester, UK, 2004.

[31] A. Badiee, R. Wildman, I. Ashcroft, Effect of UV aging on degradation of ethylene-vinyl Acetate (EVA) as encapsulant in photovoltaic (PV) modules, in: Reliability of Photovoltaic Cells, Modules, Components, and Systems VII, SPIE, 2014, p. 91790O, https://doi.org/10.1117/12.2062007.

[32] Xin Liu, 6.3 IR spectrum and characteristic absorption bands, in: Organic Chemistry, BC, Kwantlen Polytechnic University, Surrey, 2021. https://kpu.pressbooks.pub/organicchemistry/chapter/6-3-ir-spectrum-and-characteristic-absorption-bands/. (Accessed 8 August 2025).

[33] Brian C. Smith, The Carbonyl Group, Part V: Carboxylates—Coming Clean, vol. 33, 2018, pp. 20–23. https://www.spectroscopyonline.com/view/carbonyl-group-part-v-carboxylates-coming-clean. (Accessed 9 August 2025).

[34] L.L. Shevchenko, Infrared spectra of salts and complexes of carboxylic acids and some of their derivatives, Russ. Chem. Rev. 32 (1963), https://doi.org/10.1070/rc1963v032n04abeh001329.

[35] D. Kennepohl, S. Farmer, W. Reusch, 11.5: infrared Spectra of some common functional groups, Via Libre (2020). https://chem.libretexts.org/Bookshelves/Organic_Chemistry/Map%3A_Organic_Chemistry_(Wade)_Complete_and_Semesters_I_and_II/Map%3A_Organic_Chemistry_(Wade)/11%3A_Infrared_Spectroscopy_and_Mass_Spectrometry/11.05%3A_Infrared_Spectra_of_Some_Common_Functional_Groups. (Accessed 9 August 2025).

[36] J.D. Miller, J.J. Kellar, Internal reflection spectroscopy for FTIR analysis of carboxylate adsorption by semi-soluble salt minerals, in: Advances in Flotation Technology, 1999, pp. 45–58.

[37] P.J. Larkin, A. Jackson, Interpretation of the infrared Spectra of metal-stearate salts, Applied Spectroscopy Practica 2 (2024), https://doi.org/10.1177/27551857241253834.

[38] J. Almond, P. Sugumaar, M.N. Wenzel, G. Hill, C. Wallis, Determination of the carbonyl index of polyethylene and polypropylene using specified area under band methodology with ATR-FTIR spectroscopy, E-Polymers 20 (2020) 369–381, https://doi.org/10.1515/epoly-2020-0041.

[39] K. Hara, S. Jonai, A. Masuda, Crystalline Si photovoltaic modules functionalized by a thin polyethylene film against potential and damp-heat-induced degradation, RSC Adv. 5 (2015) 15017–15023, https://doi.org/10.1039/c4ra13360a.

[40] K. Hara, Y. Chiba, Spectroscopic investigation of long-term outdoor-exposed crystalline silicon photovoltaic modules, J. Photochem. Photobiol. Chem. 404 (2021), https://doi.org/10.1016/j.jphotochem.2020.112891.

[41] M. Tiefenthaler, G.M. Wallner, R. Pugstaller, Effect of global damp heat ageing on debonding of crosslinked EVA- and POE-glass laminates, Sol. Energy Mater. Sol. Cell. 264 (2024), https://doi.org/10.1016/j.solmat.2023.112602.

[42] M. Wendt, P. Wessel, R. Gottschalg, A. Mordvinkin, R. Heidrich, Crosslinking behavior of ethylene-vinyl acetate copolymer encapsulants in dependence of the additive composition, Prog. Photovoltaics Res. Appl. (2024), https://doi.org/10.1002/pip.3849.

[43] F. Gugumus, Possibilities and limits of synergism with light stabilizers in polyolefins 2. UV absorbers in polyolefins, Polym. Degrad. Stabil. 75 (2002) 309–320. www.elsevier.com/locate/polydegstab.

[44] R. Heidrich, N. Babić, O. Lacroix-Andrivet, C.E. Dutoit, C. Bainier, A. Mordvinkin, R. Gottschalg, H. Vezin, C. Afonso, S. Pondaven, From performance measurements to molecular level characterization: exploring the differences between ultraviolet and damp heat weathering of photovoltaics modules, Sol. RRL 8 (2024), https://doi.org/10.1002/solr.202400144.

[45] S.F. Chabira, M. Sebaa, C. G'Sell, Oxidation and crosslinking processes during thermal aging of low-density polyethylene films, J. Appl. Polym. Sci. 124 (2012) 5200–5208, https://doi.org/10.1002/app.34080.

[46] B. Baum, The mechanism of polyethylene oxidation, J. Appl. Polym. Sci. 2 (1959) 281–288, https://doi.org/10.1002/app.1959.070020604.

[47] R. Yang, Y. Liu, J. Yu, K. Wang, Thermal oxidation products and kinetics of polyethylene composites, Polym. Degrad. Stabil. 91 (2006) 1651–1657, https://doi.org/10.1016/j.polymdegradstab.2005.12.013.

[48] I. Bauer, W.D. Habicher, " C Rautenberg, S. Al-Malaikab, Antioxidant Interaction Between Organic Phosphites and Hindered Amine Light Stabilisers During Processing and Thermoxidation of Polypropylene, n.d.

[49] K. Schwetlick, Mechanisms of antioxidant action of phosphite and phosphonite esters, in: G. Scott (Ed.), Mechanisms of Polymer Degradation and Stabilisation, Springer Netherlands, Dordrecht, 1990, pp. 23–60, https://doi.org/10.1007/978-94-011-3838-3_2.

[50] G. Malík Ján, Ligner, Hindered amine light stabilizers: introduction, in: G. Pritchard (Ed.), Plastics Additives: an A-Z Reference, Springer Netherlands, Dordrecht, 1998, pp. 353–359, https://doi.org/10.1007/978-94-011-5862-6_38.

[51] M.C. Celina, E. Linde, E. Martinez, Carbonyl identification and quantification uncertainties for oxidative polymer degradation, Polym. Degrad. Stabil. 188 (2021), https://doi.org/10.1016/j.polymdegradstab.2021.109550.

[52] D. Wu, P. Wessel, J. Zhu, D. Montiel-Chicharro, T.R. Betts, A. Mordvinkin, R. Gottschalg, Influence of lamination conditions of EVA encapsulation on photovoltaic module durability, Materials 16 (2023), https://doi.org/10.3390/ma16216945.

[53] M.C.C. de Oliveira, A.S.A. Diniz Cardoso, M.M. Viana, V. de F.C. Lins, The causes and effects of degradation of encapsulant ethylene vinyl acetate copolymer (EVA) in crystalline silicon photovoltaic modules: a review, Renew. Sustain. Energy Rev. 81 (2018) 2299–2317, https://doi.org/10.1016/j.rser.2017.06.039.

[54] K. Thaworn, P. Buahom, S. Areerat, Effects of organic peroxides on the curing behavior of EVA encapsulant resin, Open J. Polym. Chem. 2 (2012) 77–85, https://doi.org/10.4236/ojpchem.2012.22010.

[55] J. Li, Z. Si, K. Shang, Y. Feng, S. Wang, S. Li, Kinetic and thermodynamic investigation on diffusion-limited crosslinking reaction behaviors of peroxide-induced low-density polyethylene, Polym. Test. 124 (2023), https://doi.org/10.1016/j.polymertesting.2023.108095.

[56] H. Nara, T. Miyamoto, T. Kosaki, H. Hayashi, T. Momma, Artificial solid electrolyte interphase composed of a tris(2-acryloyloxyethyl) isocyanurate-based polymer for lithium metal anode, EES Batteries (2025), https://doi.org/10.1039/d5eb00109a.

[57] A. Matsumoto, C. Hirao, K. Miyata, H. Aota, Y. Takayama, H. Toridome, Further discussion of the specific polymerization behavior of Triallyl isocyanurate. Enhanced Occurrence of Intermolecular Crosslinking at an Early Stage of Polymerization, 2002.

[58] J. Li, K. Shang, S. Wang, Y. Feng, G. Chen, S. Li, Temperature-dependent synergistic antioxidants for high-efficiency modulation of anti-scorch performance and crosslinking degree in peroxide-initiated low-density polyethylene, Mater. Lett. 362 (2024), https://doi.org/10.1016/j.matlet.2024.136211.

[59] J. Li, Z. Si, S. Wang, S. Li, H. Zhou, J. Liu, Effect of hindered phenolic antioxidants on crosslinking characteristics of low-density polyethylene initiated by peroxide, Energy Rep. 9 (2023) 159–166, https://doi.org/10.1016/j.egyr.2023.04.275.

[60] R. Heidrich, M. Ludemann, A. Mordvinkin, R. Gottschalg, Diffusion of UV additives in ethylene-vinyl acetate copolymer encapsulants and the impact on polymer reliability, IEEE J. Photovoltaics 14 (2024) 131–139, https://doi.org/10.1109/JPHOTOV.2023.3333198.

[61] J.F. Moulder, W.F. Stickle, P.E. Sobol, K.D. Bomben, J. Chastain, Handbook of X-ray Photoelectron Spectroscopy: a Reference Book of Standard Spectra for Identification and Interpretation of XPS Data, 1992.

[62] G. Säckl, G.M. Wallner, J. Duchoslav, M. Tiefenthaler, D. Stifter, XPS analysis of damp heat aged and fractured polymer/glass laminates, Polym. Test. 140 (2024), https://doi.org/10.1016/j.polymertesting.2024.108617.

[63] V. Fiandra, L. Sannino, C. Andreozzi, G. Flaminio, M. Pellegrino, New PV encapsulants: assessment of change in optical and thermal properties and chemical degradation after UV aging, Polym. Degrad. Stabil. 220 (2024), https://doi.org/10.1016/j.polymdegradstab.2023.110643.

[64] P. Gijsman, Review on the thermo-oxidative degradation of polymers during processing and in service, E-Polymers (2008) 65. http://www.e-polymers.org.

[65] M.C. Celina, Review of polymer oxidation and its relationship with materials performance and lifetime prediction, Polym. Degrad. Stabil. 98 (2013) 2419–2429, https://doi.org/10.1016/j.polymdegradstab.2013.06.024.

[66] Y. Ye, K.I. R, Additives for polyolefin film products: an overview of chemistry and effects, in: Ciba Specialty Chemicals, 2003. Tarrytown, NY.

[67] J. Lacoste, D.J. Carlsson, S. Falicki, D.M. Wiles, Polyethylene hydroperoxide decomposition products, Polym. Degrad. Stabil. 34 (1991) 309–323, https://doi.org/10.1016/0141-3910(91)90125-B.

[68] G. Park, H. Lim, D.Y. Jun, J. Moon, Z. Otgongerel, J.W. Park, J. Kim, S.H. Kim, Soldering flux causes corrosion of indium tin oxide electrode in heterojunction solar cells, Cell Rep. Phys. Sci. 6 (2025), https://doi.org/10.1016/j.xcrp.2025.102619.

[69] V. Verdingovas, M.S. Jellesen, R. Ambat, Solder flux residues and humidity-related failures in electronics: relative effects of weak organic acids used in No-Clean flux systems, J. Electron. Mater. 44 (2015) 1116–1127, https://doi.org/10.1007/s11664-014-3609-0.

[70] P. Klemchuk, Myer Ezrin, G. Lavigne, W. Halley, G. James, S. Agro, Investigation of the Degradation and Stabilization of EVA-based Encapsulant in field-aged Solar Energy Modules, 1997.

[71] M. Gardette, A. Perthue, J.L. Gardette, T. Janecska, E. Földes, B. Pukánszky, S. Therias, Photo- and thermal-oxidation of polyethylene: comparison of mechanisms and influence of unsaturation content, Polym. Degrad. Stabil. 98 (2013) 2383–2390, https://doi.org/10.1016/j.polymdegradstab.2013.07.017.

[72] S.O. Han, D.W. Lee, H. Han, Thermal degradation of crosslinked high density polyethylene, Polym. Degrad. Stabil. 63 (1999) 237.

[73] F.J. Barba, S. Roohinejad, K. Ishikawa, S.Y. Leong, A. El-Din A Bekhit, J.A. Saraiva, N. Lebovka, Electron spin resonance as a tool to monitor the influence of novel processing technologies on food properties, Trends Food Sci. Technol. 100 (2020) 77–87, https://doi.org/10.1016/j.tifs.2020.03.032.

[74] P. Gong, H. Yuan, P. Zhai, Y. Xue, H. Li, W. Dong, G. Mailhot, Investigation on the degradation of benzophenone-3 by UV/H2O2 in aqueous solution, Chem. Eng. J. 277 (2015) 97–103, https://doi.org/10.1016/j.cej.2015.04.078.

[75] X. Sun, J. Xing, Y. Yang, X. Yuan, H. Li, H. Tong, Ohimc contact Formation mechanism of silver–aluminum paste metallization on the p + emitter of n-Type crystalline silicon solar cells, J. Electron. Mater. 51 (2022) 5717–5722, https://doi.org/10.1007/s11664-022-09821-2.

[76] J. Cui, M.G. Kast, B.A. Hammann, Y. Afriyie, K.N. Woods, P.N. Plassmeyer, C. K. Perkins, Z.L. Ma, D.A. Keszler, C.J. Page, S.W. Boettcher, S.E. Hayes, Aluminum oxide thin films from aqueous solutions: insights from solid-state NMR and dielectric response, Chem. Mater. 30 (2018) 7456–7463, https://doi.org/10.1021/acs.chemmater.7b05078.

[77] Aluminium Federation Fact Sheet, Aluminium finishing. https://Www.Alfed.Org.Uk, 2020.

[78] Lifka, An improved exfoliation Test for aluminum alloys, Corrosion (1966), https://doi.org/10.5006/0010-9312-22.1.7.

[79] V. Branzoi, F. Golgovici, F. Branzoi, Aluminium Corrosion in Hydrochloric Acid Solutions and the Effect of Some Organic Inhibitors, 2002.

[80] B.C. Bunker, Molecular mechanisms for corrosion of silica and silicate glasses, J. Non-Cryst. Solids 179 (1994) 300–308.

[81] E.L. Coles, J.G. Gibson, R.M. Hinde, The corrosion of lead by dilute aqueous organic acids, J. Appl. Chem. 8 (1958) 341–348, https://doi.org/10.1002/jctb.5010080511.

[82] T. Semba, Corrosion mechanism analysis of the front-side metallization of a crystalline silicon PV module by a high-temperature and high-humidity test, Jpn. J. Appl. Phys. 59 (2020), https://doi.org/10.35848/1347-4065/ab8274.

[83] Caloritech, Technical data - galvanic corrosion, n.d. https://content.thermon.com/pdf/Caloritech/Catalog/Caloritech_Technical_Data_Corrosion.pdf (accessed August 19, 2025).

[84] Galvanic series of metals and alloys in seawater, in: S.D. Cramer, B.S. Covino Jr. (Eds.), Corrosion: Materials, ASM International, 2018, https://doi.org/10.31399/asm.hb.v13b.a0003796, 672–672.

[85] A. Zaki, Basic concepts in corrosion, in: Principles of Corrosion Engineering and Corrosion Control, first ed., Butterworth–Heinemann (Elsevier), 2006, pp. 750–780, https://doi.org/10.1016/B978-0-7506-5924-6.00002-5.